Editors' Suggestion

Probing orbits of stellar mass objects deep in galactic nuclei with quasiperiodic eruptions

Cong Zhou,[1,3,*] Lei Huang,[2,4] Kangrou Guo,[5] Ya-Ping Li,[2,4] and Zhen Pan[5,6,†]

[1]*CAS Key Laboratory for Research in Galaxies and Cosmology, Department of Astronomy, University of Science and Technology of China, Hefei 230026, People's Republic of China*
[2]*Shanghai Astronomical Observatory, Chinese Academy of Sciences, 80 Nandan Road, Shanghai 200030, People's Republic of China*
[3]*School of Astronomy and Space Sciences, University of Science and Technology of China, Hefei 230026, People's Republic of China*
[4]*Key Laboratory for Research in Galaxies and Cosmology, Chinese Academy of Sciences, Shanghai 200030, People's Republic of China*
[5]*Tsung-Dao Lee Institute, Shanghai Jiao-Tong University, Shanghai, 520 Shengrong Road, 201210, People's Republic of China*
[6]*School of Physics and Astronomy, Shanghai Jiao-Tong University, Shanghai, 800 Dongchuan Road, 200240, People's Republic of China*

(Received 28 January 2024; accepted 15 April 2024; published 20 May 2024)

Quasiperiodic eruptions (QPEs) are intense, repeating, soft x-ray bursts with recurrence times of about a few to ten hours from nearby galactic nuclei. The origin of QPEs is still unclear. In this work, we investigate the extreme mass ratio inspiral (EMRI) + accretion disk model, where the disk is formed from a previous tidal disruption event (TDE). In this EMRI + TDE disk model, the QPEs are the result of collisions between a TDE disk and a stellar mass object (a stellar mass black hole or a main sequence star) orbiting around a supermassive black hole (SMBH) in galactic nuclei. If this interpretation is correct, QPEs will be invaluable in probing the orbits of stellar mass objects in the vicinity of SMBHs and further inferring the formation of EMRIs, which are one of the primary targets of spaceborne gravitational wave missions. Taking GSN 069 as an example, we find the EMRI that is of low eccentricity ($e < 0.1$ at the 3-σ confidence level) and a semimajor axis about $O(10^2)$ gravitational radii of the central SMBH, which is consistent with the prediction of the wet EMRI formation channel while incompatible with alternatives.

DOI: 10.1103/PhysRevD.109.103031

I. INTRODUCTION

In the past decade, x-ray quasiperiodic eruptions (QPEs) have been detected in nearby galactic nuclei [1–5] which host low-mass ($\simeq 10^5$–$10^7 M_\odot$ at most) central supermassive black holes (SMBHs) [6,7]. QPEs are fast, bright, soft x-ray bursts repeating every few hours with peak x-ray luminosity of 10^{42}–10^{43} ergs s^{-1}. QPEs have thermal-like x-ray spectra with temperatures in the range $kT \simeq 100$–250 eV, in contrast with the temperatures $\simeq 50$–80 eV in the quiescent state. The presence of a narrow line region in all QPE host galaxies implies that a long-lived active galactic nucleus (AGN) likely plays an integral role in the QPEs, while the absence of luminous broad emission lines indicates that none of the central SMBHs is currently actively accreting; i.e., they are likely all recently switched-off AGNs [6]. In addition, QPEs similar to tidal disruption events (TDEs) are preferentially found in post-starburst galaxies [6], and two QPE sources (GSN 069 and XMMSL1 J024916.6-04124) and a candidate (AT 2019vcb) were found to be directly associated with x-ray TDEs [5,7–10]. A recent XMM-Newton observation of GSN 069 identified the reappearance of QPEs after being absent for two years [7]. This observation shows that QPEs may only be present below a quiescent luminosity threshold $L_{\rm thr} \sim 0.4 L_{\rm Edd}$, where $L_{\rm Edd}$ is the Eddington luminosity, and a new phase shows up in the QPE reappearance where the intensity and the temperature of two QPEs become different. Long-term observations yield more interesting features of GSN 069 [11]; e.g., the quasiperiodic oscillations (QPOs) in the quiescent state following the QPEs, long-term evolution of the quiescent level emission consistent with a TDE or even possibly a repeating TDE, and QPEs measured in higher energy bands, which are stronger, peak earlier, and have shorter duration than when measured at lower energies.

Many models have been proposed for explaining the physical origin of QPEs, based on different disk

*dysania@mail.ustc.edu.cn
†zhpan@sjtu.edu.cn

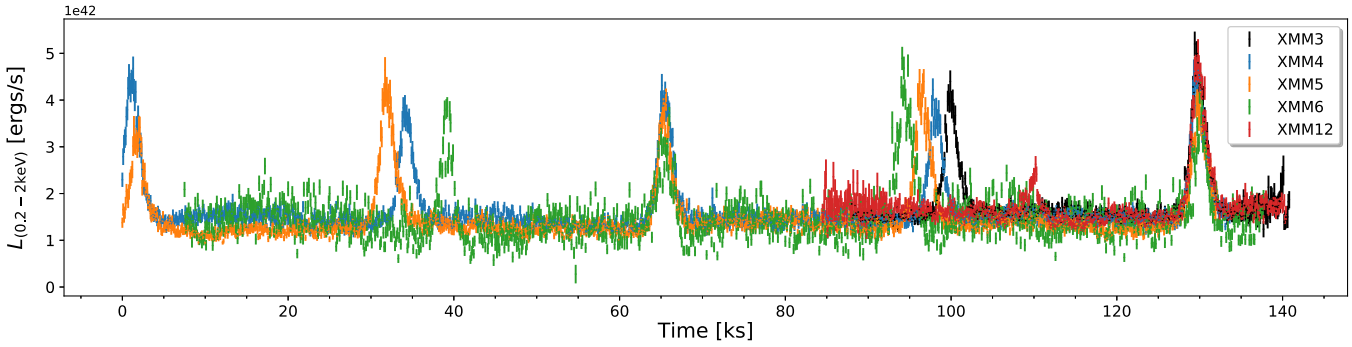

FIG. 1. QPE light curves from observations XMM 3–6 and 12, where we have aligned different observations at their last peak locations and also rescaled the XMM 6 luminosity.

instabilities[1] [13–17], self-lensing binary massive black holes [18], mass transfer at the pericenter from stars or white dwarfs orbiting around the SMBH [19–28], (periodic) impacts between a stellar-mass object (SMO), a star or a stellar mass black hole (sBH), and the accretion disk that is formed following a recent TDE (dubbed the EMRI + TDE disk model) [29–33]. These models can explain some of the features in the QPE light curves (mainly GSN 069); there is no model that produces diverse features of different QPE sources (see more discussions in, e.g., Refs. [2–7,11,34]).

Recently, Linial *et al.* [32] and Franchini *et al.* [33] pointed out that the EMRI + TDE disk model is flexible in recovering comprehensive features of different QPEs. In this EMRI + TDE disk model, the stellar mass object (SMO) could be a sBH or a main sequence star, and the two share many similar model predictions, e.g., the long-short pattern in the QPE recurrence times and the strong-weak pattern in the QPE intensities (see [32,33,35] for details); therefore, it seems hard to distinguish the two with the existing QPE observations. In the majority of this work, we tend not to distinguish them, and we will briefly discuss the different predictions that might be tested by near future observations in the final part of this paper. We first refine the flare model following the analytic supernova explosion model developed by Arnett [36] and used in modeling the optical flares of OJ 287 [37,38] and SDSSJ1430 + 2303 [39]. With this refinement, we find the model fitting to the QPE light curves with reasonable precision, though the effective temperatures at the light curve peaks in the best-fit model are in mild tension with the observation values. Because of this limitation of the plasma ball emission model, we consider an alternative phenomenological model where the light curve consists of a rising part and a decay part with different timescales. We apply both models to the QPEs from GSN 069 and find the starting time of each flare, with which we constrain the EMRI orbital parameters. We find the EMRI orbit inferred from these QPEs is of low eccentricity ($e < 0.1$ at the 3-σ confidence level) and semimajor axis $a = \mathcal{O}(10^2)M_\bullet$, where $M_\bullet$ is the gravitational radius of the central SMBH. If the EMRI + TDE disk is indeed the origin of QPEs, the EMRI orbital parameters inferred from the QPEs will be invaluable in probing the EMRI formation channels. As for the GSN 069 EMRI, we find it is highly unlikely that it comes from the loss-cone channel or the Hills mechanism, while is consistent with the wet channel expectation (see Figs. 5 and 6).

This paper is organized as follows. In Sec. II, we briefly review the flare emission mechanism, introduce two analytic models for fitting the QPE light curves and the EMRI equations of motion (EOM). In Sec. III, we fit the QPE light curves and find the starting time of each flare, with which we constrain the EMRI orbital parameters. In Sec. IV, we summarize this paper by evaluating the performance of the EMRI + disk model predictions, discussing the implications of QPEs on EMRI formation channels, possible observable signatures for distinguishing stellar EMRIs versus sBH EMRIs, and future work. In Appendix A, we include the detailed corner plots of emission model parameters and the flare timing model parameters. In Appendix B, we analyze the orbital stability of the SMO after a possible close-by scattering with a TDE remnant star. In Appendix C, we show some hydrodynamic (HD) simulation results of SMO-disk collisions and infer possible observational features in the resulting light curves. In this paper, we use geometrical units with $G = c = 1$ if not specified otherwise.

II. QPE MODEL: EMRI + TDE DISK

Figure 1 displays the GSN 069 QPEs found in five XMM Newton observations. The peak luminosity, recurrence time, and duration of QPEs are $\mathcal{O}(10^{42})$ ergs/s, $\mathcal{O}(10)$ hours, and $\mathcal{O}(1)$ hour, respectively. In this section, we first sketch the EMRI + TDE disk model, identifying the parameter space that is consistent with the above energy budget and timescales; then, we explain the details of the

[1]The classical limit-cycle instability in AGN disks is disfavored because the QPE periods, burst timescales, and burst profiles cannot be reconciled with the limit-cycle prediction [3,12].

emission models for fitting each individual QPE light curve and the EMRI model for fitting the starting times of all QPEs.

A. Emission model

As the SMO orbits around the SMBH and crosses the accretion disk, the relative velocity between the SMO and the local accretion flow, in general, is higher than the local sound speed $v_{\rm vel} > c_{\rm s}$, and the gas in the disk will be compressed and heated by the shock wave. For sBHs, the accretion radius $r_{\rm acc} \coloneqq 2Gm/v_{\rm rel}^2$ is, in general, much larger than the geometrical size m. As shown by simulations in Ref. [40], the heated gas expands along the shocked tunnel and forms a hot, optically thick, radiation-dominated plasma ball on each side of the disk. The hot plasma ball cools down due to (nearly) adiabatic expansion and thermal radiation. For stars, the whole process is similar except now the geometrical radius $R_\star$ plays the role of the accretion radius in the sBH case.

We consider the standard α disk model [41], where the disk structure in the radiation-dominated regime can be analytically expressed as [42]

$$\begin{aligned}\Sigma(r) &= 1.7\times 10^5\ {\rm g\,cm^{-2}}\alpha_{0.01}^{-1}\dot{M}_{\bullet,0.1}^{-1}r_{100}^{3/2},\\ H(r) &= 1.5M_\bullet\dot{M}_{\bullet,0.1},\end{aligned}\tag{1}$$

where H is the scale height of the disk from the midplane, Σ is the disk surface density, and we have defined $\alpha_{0.01}=\alpha/0.01, r_{100}=r/100M_\bullet, \dot{M}_{\bullet,0.1}=\dot{M}_\bullet/(0.1\dot{M}_{\bullet,\rm Edd})$, with $\dot{M}_{\bullet,\rm Edd}$ the Eddington accretion rate. The disk surface density and the disk thickness will be used in the energy budget estimates and the EMRI orbit inference.

For a star, the energy loss after crossing a disk is simply

$$\begin{aligned}\delta E_\star &= 2\times\frac{1}{2}\delta m_{\rm gas}v_{\rm rel}^2\\ &\approx 3\times 10^{46}\ {\rm ergs}\times\Sigma_5 R_{\star,\odot}^2 r_{100}^{-1}\sin\iota_{\rm sd},\end{aligned}\tag{2}$$

where the factor 2 in the first line takes both the thermal energy and the kinetic energy of the shocked gas into account, $\Sigma_5 \coloneqq \Sigma/(10^5\ {\rm g\,cm^{-2}}), R_{\star,\odot}\coloneqq R_\star/R_\odot$, $\delta m_{\rm gas}=2\pi R_\star^2\Sigma/\sin\iota_{\rm sd}$ is the mass of the shocked gas [32], and we have used the approximation $v_{\rm vel}\approx v_{\rm K}\sin\iota_{\rm sd}$, with $v_{\rm K}$ the local Keplerian velocity, where $\iota_{\rm sd}$ is the angle between the sBH orbital plane and the disk plane.

For a sBH moving in a uniform gas cloud, the gravitational drag from the perturbed gas is [43–46]

$$\begin{aligned}\mathbf{F}_{\rm drag} &= -4\pi\ln\Lambda\frac{G^2\rho m^2}{v_{\rm rel}^3}\left[{\rm erf}(X)-\frac{2X}{\sqrt{\pi}}e^{-X^2}\right]\mathbf{v}_{\rm rel}\\ &\approx -4\pi\ln\Lambda\frac{G^2\rho m^2}{v_{\rm rel}^3}\mathbf{v}_{\rm rel},\end{aligned}\tag{3}$$

where ρ is the gas density, m is the sBH mass, $X=v_{\rm rel}/(\sqrt{2}c_s)$ is the ratio of the relative velocity $v_{\rm rel}$ over the gas particle velocity dispersion (approximated by the local sound speed c_s), and we have used the approximation $v_{\rm rel}/c_s\gg 1$ in the second line; $\ln\Lambda=\ln(b_{\rm max}/b_{\rm min})$ is the Coulomb logarithm, with $b_{\rm max/min}$ the maximum/minimum cutoff distance associated with the interaction. The cutoff distance $b_{\rm max}$ is the maximum extent of the wake $2H\sin^{-1}\iota_{\rm sd}$, while $b_{\rm min}$ is identified either as the accretor size m [47–50] or as the standoff distance $r_{\rm so}\approx\frac{1}{2}r_{\rm acc}$ [51]. With these two different identifications, we have $\ln\Lambda\approx 13$ or 5, where we have used the fiducial values $M_\bullet=10^6M_\odot$, $m=30M_\odot, H=1.5M_\bullet$, and $\sin\iota_{\rm sd}=0.1$ in the approximately equal sign. As a result, the sBH loses energy after crossing a disk,[2]

$$\begin{aligned}\delta E_{\rm sBH} &= F_{\rm drag}\Delta L = 4\pi\ln\Lambda\frac{G^2m^2}{v_{\rm rel}^2}\frac{\Sigma}{\sin(\iota_{\rm sd})}\\ &\approx 2\times 10^{46}\ {\rm ergs}\left(\frac{\ln\Lambda}{10}\right)\Sigma_5 m_{30}^2 r_{100}\left(\frac{\sin\iota_{\rm sd}}{0.1}\right)^{-3},\end{aligned}\tag{4}$$

where $\Delta L=2H/\sin(\iota_{\rm sd})$ is the length of the sBH orbit inside the disk, and we have defined $m_{30}=m/30M_\odot$.

In order to find the starting time of each flare, we consider the following two emission models: an expanding plasma ball emission model and a phenomenological model.

1. Plasma ball model

In general, the postshock gas is not uniformly compressed, heated, or accelerated depending on where it crosses the shock front (see, e.g., Refs. [48,52–55] for detailed simulations). For modeling the emission of the shocked gas, we simplify the shocked gas as a uniform plasma ball with initial size R_0 and initial surface temperature $T_{\rm e0}$. Following Arnett [36], we model the plasma ball expansion, cooling, and radiation as follows.

Considering a spherical plasma ball expanding uniformly, the evolution of the expanding shell follows the first law of thermodynamics, which states, in Lagrangian coordinates,

$$\dot{E}+P\dot{V}=-\frac{\partial L}{\partial m},\tag{5}$$

[2]In estimating the sBH energy loss in crossing the disk, one can easily use the approximation $\delta E_{\rm sBH}=\frac{1}{2}\delta m_{\rm gas}v_{\rm rel}^2$. In fact, $\delta m_{\rm gas}$ is merely the amount of gas that is supposed to be accreted by the sBH, which is only a fraction of the shocked gas (the shock size is larger than the accretion radius $r_{\rm acc}$ by quite a few times (see, e.g., Refs. [48,52–55]). A more accurate estimate of the sBH energy loss is Eq. (4), which was derived in Ref. [44] and verified with hydrodynamic simulations (see, e.g., Refs. [47,48,50,54,55]).

where E and V are the specific energy and volume, P and L are the pressure and the radiation luminosity, and m is the total mass enclosed by the shell we consider. In the diffusion approximation, L is

$$\frac{L}{4\pi r^2} = -\frac{ac}{3\kappa\rho}\frac{\partial T^4}{\partial r}, \tag{6}$$

where κ is the opacity dominated by Thomson scattering.

Adiabatic homologous expansion of a photon-dominated gas ($\gamma = 4/3$) gives $T \propto R(t)^{-1}$ and $\rho(t) \propto R(t)^{-3}$, where $R(t)$ is the boundary of the plasma ball. With these two relations, we can now write

$$T(x,t)^4 = \Psi(x)\phi(t)T_{00}^4\frac{R_0^4}{R(t)^4}, \tag{7}$$

$$\rho(t) = \rho_0\frac{R_0^3}{R(t)^3}, \tag{8}$$

$$\frac{\dot{V}}{V} = 3\frac{\dot{R}}{R}, \tag{9}$$

where $x = r/R(t)$ is a dimensionless comoving radial coordinate. In the timescale we are considering, the outer boundary of the plasma ball expands at a constant speed,

$$R(t) \equiv R_0\left(1+\frac{t}{\tau_h}\right) = R_0 + v_{sc}t, \tag{10}$$

where τ_h is the expansion timescale and $v_{sc} = R_0/\tau_h$ is the expanding velocity scale. In Eq. (7), we separate the space and time dependence of temperature.

Plugging Eqs. (6)–(9) into Eq. (5) and separating the PDE, we have

$$\alpha = -\frac{1}{x^2\Psi}\frac{\mathrm{d}}{\mathrm{d}x}\left(x^2\frac{\mathrm{d}\Psi}{\mathrm{d}x}\right), \tag{11}$$

$$\frac{\mathrm{d}\phi}{\mathrm{d}t} = -\frac{R(t)\phi}{R_0\tau_0}, \tag{12}$$

where α is the eigenvalue determined by the boundary condition and $\tau_0 \equiv \frac{3\rho_0 R_0^2\kappa}{\alpha c}$ is the diffusion timescale. We consider the "radiative zero" boundary condition [36] [$\Psi(1) = 0$]. Together with the trivial boundary condition at the center, $\Psi(0) = 1, \mathrm{d}\Psi/\mathrm{d}x = 0$, the solution to Eq. (11) is

$$\Psi(x) = \frac{\sin(\pi x)}{\pi x}, \tag{13}$$

with the eigenvalue $\alpha = \pi^2$. The time evolution equation (12) can be solved with the trivial initial condition $\phi(0) = 1$, whose solution is

$$\phi(t) = \exp\left[-\frac{t}{\tau_0}\left(1+\frac{t}{2\tau_h}\right)\right]. \tag{14}$$

With Eqs. (10), (13), and (14), the temperature distribution and evolution are obtained. We now return to the surface luminosity. Plugging Eqs. (7), (10), (13), and (14) into Eq. (6) and taking $x = 1$, we have

$$L(1,t) = \frac{4\pi R_0 a T_{00}^4 c}{3\kappa\rho_0}\phi(t) \equiv L(1,0)\phi(t). \tag{15}$$

Next, we choose the effective temperature as the parameter of our model, which can be directly obtained from the surface luminosity

$$T_{\mathrm{e}} = \left(\frac{L(1,0)}{4\pi\sigma R_0^2}\right)^{1/4}\phi^{1/4}\Big/\sqrt{1+\frac{t}{\tau_h}} \equiv T_{\mathrm{e}0}\phi^{1/4}\Big/\sqrt{1+\frac{t}{\tau_h}}. \tag{16}$$

Applying this model to QPEs, we find the soft x-ray (0.2–2 keV) luminosity

$$L_X = \frac{8\pi^2 h R^2}{c^2}\int_{0.2\ \mathrm{keV}}^{2\ \mathrm{keV}}\frac{\nu^3 d\nu}{e^{h\nu/k_B T_{\mathrm{e}}}-1}, \tag{17}$$

where the effective temperature T_{e} is determined by Eq. (16) and the plasma ball radius R is determined by Eq. (10). The intrinsic parameters of our model are $\{R_0, T_{\mathrm{e}0}, \tau_0, \tau_h\}$ in addition to the flare staring time t_0. For the purpose of model parameter inference, we find that parameters $\{t_0, R_0, T_{\mathrm{e}0}, \tau_m \coloneqq \sqrt{\tau_0\tau_h}, v_{sc} \coloneqq R_0/\tau_h\}$ are better constrained, so they are chosen as the model intrinsic parameters hereafter.

2. Phenomenological model

In additional to the above expanding plasma ball emission model, we also consider the following alternative phenomenological light curve model [4,56],

$$L_{\mathrm{X}}(t) = \begin{cases} 0 & \text{if } t \le t_p - t_{\mathrm{as}} \\ L_p e^{\sqrt{\tau_1/\tau_2}} e^{\tau_1/(t_p - t_{\mathrm{as}} - t)} & \text{if } t_p - t_{\mathrm{as}} < t < t_p \\ L_p e^{-(t-t_p)/\tau_2} & \text{if } t \ge t_p, \end{cases} \tag{18}$$

where $t_{\mathrm{as}} = \sqrt{\tau_1\tau_2}$. Following Ref. [56], we define the flare starting time as the time when the flux is $1/e^3$ of the peak value, i.e., $L_{\mathrm{X}}(t_0) = L_p/e^3$. Therefore, only three out of the four time variables are independent, and we take $\{t_0, t_p, \tau_2\}$ and L_p as the independent model parameters.

In addition to the QPEs, QPOs have been identified in the quiescent state luminosity; we therefore model the background luminosity as

$$L_{\mathrm{bgd}}(t) = B + A\sin\left(2\pi(t-t_0)/P_{\mathrm{QPO}} + \phi_{\mathrm{QPO}}\right), \tag{19}$$

where B is the average background luminosity, and A, $P_{\rm QPO}$, and $\phi_{\rm QPO}$ are the QPO amplitude, period, and initial phase, respectively.

B. Flare timing

In general, the sBH collides with the accretion twice per orbit, and the propagation times of the two flares produced by the collisions to the observer are different due to different propagation paths.

For convenience, we model the motion of the sBH as a geodesic in the Schwarzschild spacetime. Considering an orbit with semimajor axis a and eccentricity e, the pericenter and apocenter distances $r_{\rm a,p} = a(1 \pm e)$ are the roots to the effective potential [57],

$$V(r) = r^4E^2 - (r^2 - 2r)(r^2 + L^2), \tag{20}$$

where all the radii or distances are formulated in units of the gravitational radius $M_\bullet$. From the effective potential, it is straightforward to obtain the orbital energy and angular momenta $E(a,e), L(a,e)$. The EOMs in the Schwarzschild spacetime can be derived from the Hamiltonian

$$\mathcal{H}(r,\theta,p_r,p_\theta) = \frac{1}{2}g^{\mu\nu}(r,\theta)p_\mu p_\nu, \tag{21}$$

where $g^{\mu\nu}$ is the Schwarzschild metric. Considering the simple case where the orbit lies on the equator, we obtain

$$\begin{aligned}
\dot{r} &= \left(1 - \frac{2}{r}\right)p_r\left(\frac{dt}{d\tau}\right)^{-1}, \\
\dot{\psi} &= \frac{L}{r^2}\left(\frac{dt}{d\tau}\right)^{-1}, \\
\dot{p}_r &= -\left(\frac{p_r^2}{r^2} - \frac{L^2}{r^3} + \frac{E^2}{(r-2)^2}\right)\left(\frac{dt}{d\tau}\right)^{-1},
\end{aligned} \tag{22}$$

where $dt/d\tau = E/(1-2/r)$ and dots are the derivative with respect to time t and ψ is the azimuth angle. Combining this with the initial condition $(r,\psi,p_r)|_{t=t_{\rm ini}} = (r_{\rm a},0,0)$ (i.e., starting from the apocenter), we obtain the orbital motion $r(t)$, $\psi(t)$.

Assuming the accretion disk lies on the equator $x-y$ plane (the disk angular momentum is in the z direction, i.e., $\vec{n}_{\rm disk} = \vec{e}_z$), the orbital plane lies on the $x'-y'$ plane, and the two coordinate frames are related by Euler rotations $R_z(\gamma)R_x(\beta)R_z(\alpha)$, where

$$R_z(\alpha) = \begin{bmatrix} \cos\alpha & -\sin\alpha & \\ \sin\alpha & \cos\alpha & \\ & & 1 \end{bmatrix} \tag{23}$$

and

$$R_x(\beta) = \begin{bmatrix} 1 & & \\ & \cos\beta & -\sin\beta \\ & \sin\beta & \cos\beta \end{bmatrix}. \tag{24}$$

The orbital motion in the two frames is

$$(x',y',z') = r(\cos\psi, \sin\psi, 0) \tag{25}$$

and

$$(x,y,z)^{\rm T} = R_z(\gamma)R_x(\beta)R_z(\alpha)(x',y',z')^{\rm T}, \tag{26}$$

respectively. Specifically, β is the angle between the disk plane and the orbital plane, i.e., $\iota_{\rm sd} = \min\{\beta, \pi - \beta\}$.

We use a coordinate frame such that the line of sight (LOS) lies in the $x-z$ plane with $\vec{n}_{\rm los} = (\sin\theta_{\rm los}, 0, \cos\theta_{\rm los})$. The observable collisions happen when $z(t) = \pm H$, where the $\pm$ sign depends on whether the observation is on the upper or lower half plane. The propagation times of different flares at different collision locations $r_{\rm crs}\vec{n}_{\rm crs}$ to the observer will also be different. We can write $t_{\rm obs} = t_{\rm crs} + \delta t_{\rm geom} + \delta t_{\rm shap}$, where

$$\begin{aligned}
\delta t_{\rm geom} &= -r_{\rm crs}\vec{n}_{\rm los}\cdot\vec{n}_{\rm crs}, \\
\delta t_{\rm shap} &= -2M_\bullet \ln[r_{\rm crs}(1 + \vec{n}_{\rm los}\cdot\vec{n}_{\rm crs})]
\end{aligned} \tag{27}$$

are corrections caused by different path lengths and different Shapiro delays [58], respectively.

To summarize, there are eight parameters in the flare timing model: the intrinsic orbital parameters (a,e), the extrinsic orbital parameters (α,β,γ), the LOS angle $\theta_{\rm los}$, the time $t_{\rm ini}$ at the apocenter right before the first flare is observed, and the mass of the SMBH $M_\bullet$ or, equivalently, the Newtonian orbital period $T_{\rm obt} \coloneqq 2\pi(a/M_\bullet)^{3/2}M_\bullet$. Without loss of generality, we set $\theta_{\rm los} \le \pi/2$ (i.e., the observer is located in the upper half plane), and the observed flares start when the EMRI crosses the upper surface of the disk $z = H$ (we set the disk thickness as $H = 1.5M_\bullet$).

III. APPLYING THE EMRI + TDE DISK MODEL TO GSN 069 QPEs

For a given EMRI system and a TDE accretion disk, we can, in principle, predict the collision times between the SMO and the disk, the initial condition of the plasma ball from each collision, and the resulting QPE light curve. Both the EMRI orbital parameters and the disk model parameters can be constrained simultaneously from the QPE light curves. In this work, we choose to constrain the EMRI kinematics and the plasma ball emission separately: We first fit each QPE with the flare model and obtain the starting time of each flare $t_0 \pm \sigma(t_0)$, which is identified as the observed disk crossing time. In this way, the EMRI kinematics is minimally plagued by the uncertainties in the

TABLE I. Median values and 1-σ uncertainties of the flare starting times t_0 [s], the QPO periods $P_{\rm QPO}$ [ks], and the intervals $T_{\rm short,long,sum}$ [s] of GSN 069 QPEs in XMM 3–6 assuming the plasma ball model.

Plasma ball model	t_0	$P_{\rm QPO}$	$T_{\rm short}$	$T_{\rm long}$	$T_{\rm sum}$
XMM3 flare 1	662030843^{+91}_{-86}	$51^{+8.53}_{-9.91}$	29820^{+123}_{-126}		
2	662060666^{+67}_{-62}	$48^{+9.24}_{-11.39}$			
XMM4 flare 1	664003075^{+105}_{-82}	$34^{+5.84}_{-7.17}$	31448^{+99}_{-98}	32648^{+96}_{-99}	64092^{+74}_{-68}
2	664035779^{+87}_{-89}	$26^{+1.18}_{-1.07}$			
3	664066973^{+89}_{-85}	$44^{+6.26}_{-4.20}$			
4	664099564^{+84}_{-75}	$53^{+4.87}_{-6.98}$			
5	664131264^{+92}_{-87}	$32^{+6.54}_{-6.95}$			
XMM5 flare 1	675727215^{+188}_{-130}	$21^{+3.44}_{-2.31}$	30393^{+124}_{-132}	33519^{+104}_{-101}	63915^{+92}_{-106}
2	675756904^{+90}_{-87}	$31^{+1.65}_{-1.41}$			
3	675790441^{+79}_{-78}	$52^{+7.48}_{-7.67}$			
4	675821554^{+105}_{-98}	$33^{+2.29}_{-1.84}$			
5	675855051^{+83}_{-78}	$43^{+11.41}_{-10.75}$			
XMM6 flare 1	695049958^{+154}_{-142}	$43^{+1.70}_{-1.37}$	28567^{+260}_{-245}	36382^{+236}_{-255}	64935^{+250}_{-249}
2	695076440^{+132}_{-161}	$13^{+0.76}_{-0.62}$			
3	695104985^{+163}_{-141}	$30^{+4.48}_{-2.76}$			
4	695141378^{+132}_{-166}	$32^{+6.70}_{-7.23}$			
XMM12 flare 1	773633586^{+181}_{-210}	$61^{+7.31}_{-7.56}$	20069^{+223}_{-196}		
2	773653655^{+74}_{-71}	$27^{+3.78}_{-2.32}$			

disk model because the disk crossing time inferred from the QPE light curve is not expected to be sensitive to the disk model.

According to the Bayes theorem, the posterior of parameters is

$$\mathcal{P}(\mathbf{\Theta}|d) \propto \mathcal{L}(d|\mathbf{\Theta})\pi(\mathbf{\Theta}), \tag{28}$$

where $\mathcal{L}(d|\mathbf{\Theta})$ is the likelihood of detecting data d given a model with parameters $\mathbf{\Theta}$ and $\pi(\mathbf{\Theta})$ is the parameter prior assumed. For the emission model, the likelihood is defined as

$$\mathcal{L}_{\rm emission}(d|\mathbf{\Theta}) = \prod_i \frac{1}{\sqrt{2\pi(F\sigma_i)^2}} \exp\left\{-\frac{(L(t_i)-d_i)^2}{2(F\sigma_i)^2}\right\}, \tag{29}$$

where d_i, σ_i are the measured QPE luminosity and error bar at t_i, respectively, $L(t_i) = L_X(t_i) + L_{\rm bgd}(t_i)$ is the model predicted luminosity [Eqs. (17) and (19)], and F is a scale factor taking possible calibration uncertainty into account. Therefore, we have model parameters $\mathbf{\Theta} = \{t_0, R_0, T_{\rm e0}, \tau_m, v_{\rm exp}, B, A, P_{\rm QPO}, \phi_{\rm QPO}, F\}$ for each flare in the expanding plasma ball model, and $\mathbf{\Theta} = \{t_0, t_p, \tau_2, L_p, B, A, P_{\rm QPO}, \phi_{\rm QPO}, F\}$ for each flare in the phenomenological model. The posterior $t_0 \pm \sigma(t_0)$ of each flare is then fed into the flare timing model.

For the flare timing model, the likelihood is defined in a similar way as

$$\mathcal{L}_{\rm timing}(d|\tilde{\mathbf{\Theta}}) = \prod_k \frac{1}{\sqrt{2\pi(F_t\sigma(t_0^{(k)}))^2}} \exp\left\{\frac{(t_{\rm obs}^{(k)} - t_0^{(k)})^2}{2(F_t\sigma(t_0^{(k)}))^2}\right\}, \tag{30}$$

where $t_{\rm obs}^{(k)}$ is the model's predicted starting time of the kth flare in the observer's frame [Eq. (27)], and $t_0^{(k)}$ and $\sigma(t_0^{(k)})$ are the flare starting time and the uncertainty of the kth flare (see Table I). In the same way, we have included a scale factor F_t taking possible systematics and unmodeled physics processes into consideration. Therefore, we have parameters $\tilde{\mathbf{\Theta}} = \{a, e, \alpha, \beta, \gamma, T_{\rm obt}, t_{\rm ini}, \theta_{\rm obs}, F_t\}$ in the flare timing model. The model parameter inferences are performed using the dynesty [59] and nessai [60] algorithms in the Bilby package [61].

A. GSN 069 QPE light curves

GSN 069 is the first QPE source discovered, and it has been monitored extensively in the past decade, including XMM 1–12 and Chandra [7,11]. From the quiescent state light curves, it is likely that two (partial) TDEs have occurred. QPEs are found only in XMM 3–6 and 12 and the Chandra observation, when the quiescent state luminosity is low.

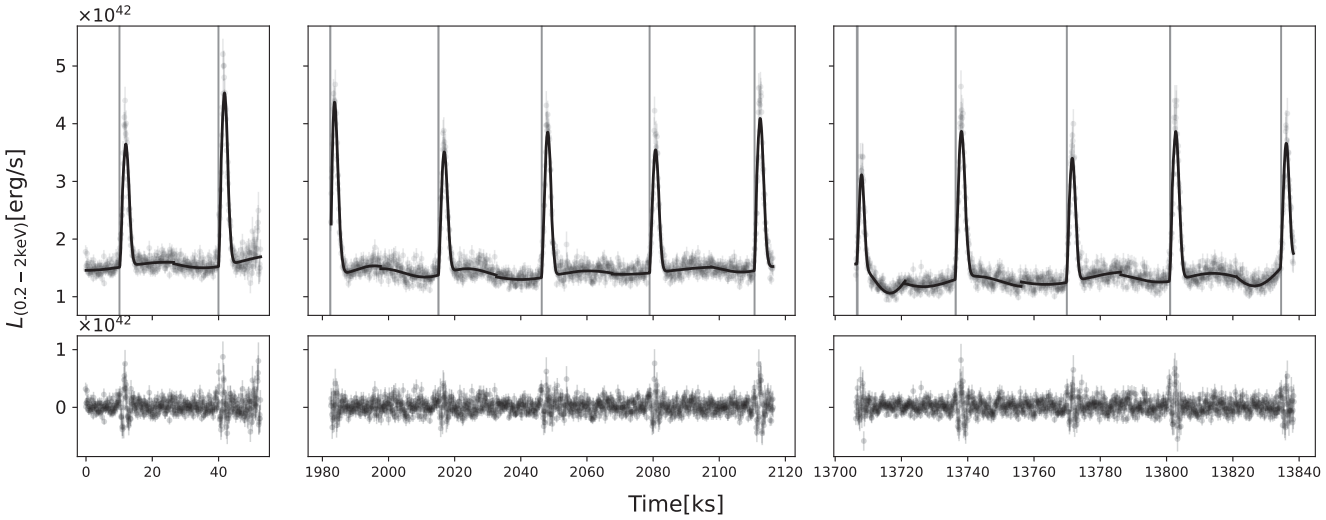

FIG. 2. Top panel: all the light curve data from XMM3-5 and the best-fit results (solid lines). Vertical bands denote the flare starting times t_0. Bottom panel: residues of the best fit. We have changed the reference time to the starting time of the XMM3 observation.

We reprocessed the raw data from the EPIC-pn camera [62] of the XMM-Newton mission, using the latest XMM–Newton Science Analysis System (SAS) and the Current Calibration Files (CCF). The photon arrival times are all barycenter-corrected in the DE405-ICRS reference system. The count-rate-luminosity conversion is accomplished with XSPEC [63]. The resulting light curves are shown in Fig. 1.[3]

During XMM 3–5 and Chandra (regular phase), the quiescent state luminosity slowly declines, and the QPEs show a clear long-short pattern in the occurrence times and a strong-weak pattern in the intensities. During XMM 6, the quiescent state luminosity likely increases in the rising phase of the second TDE, and the QPEs become irregular in the sense that the alternating strong-weak pattern is not well preserved, where the first flare does not fit in either the strong or the weak ones, though flares 2–4 still follow the alternating long-short and strong-weak patterns (see Fig. 1). During the recent observation epoch XMM 12, only two QPEs were detected, limited by the short exposure time, and it is unclear whether the QPEs have settled into a new regular phase or not.

From Fig. 1, it is evident that there is an alternating long-short pattern in the QPE recurrence times with $T_{\rm long} - T_{\rm short} \approx 2 \sim 8$ ks, and $T_{\rm long} + T_{\rm short}$ is approximately a constant. To quantify these features, we fit the QPEs with the two flare models. In Fig. 2, we show the 0.2–2 keV light curves of GSN 069 QPEs from XMM 3–5 along with the best-fit emission model (see the corner plot of the model parameter posterior in Fig. 8). From the residue plots in the lower panels, we see that the fits are reasonable for the majority of the light curves except around the peaks where the sharp turnovers are not captured by the fits, and around the flare staring times t_0 where the precursor-like features prior to the main flares cannot be captured either. These limitations also motivate us to consider the alternative phenomenological light curve model [Eq. (18)]. In Fig. 3, we show the results of the best-fit phenomenological model, which largely improves the residues around the light curve peaks and yields flare starting times t_0 consistent with those from the plasma ball model. The residues that stand out around the flare starting times imply possible processes that are not modeled in either model (see discussion in Appendix C where we conduct hydrodynamic simulations of SMO-disk collisions, trying to identify the unmodeled processes by comparing the simulations with the light curves).

In Tables I and II, we list all the flare starting times t_0, the QPO periods $P_{\rm QPO}$, and the intervals $T_{\rm short,long,sum}$ fitted from the QPE light curves with the plasma ball model and the phenomenological model, respectively. With the flare starting times $t_0^{(k)}$, we quantify the long-short pattern in the QPE recurrence times. In XMM 3, two flares are observed; therefore, only the short time $T_{\rm short}$ can be calculated. In XMM 4, five flares are observed, and we define

$$\begin{aligned} T_{\rm long} &= \frac{1}{2}\left(t_0^{(2)} - t_0^{(1)} + t_0^{(4)} - t_0^{(3)}\right)_{\rm XMM4}, \\ T_{\rm short} &= \frac{1}{2}\left(t_0^{(3)} - t_0^{(2)} + t_0^{(5)} - t_0^{(4)}\right)_{\rm XMM4}, \\ T_{\rm sum} &= T_{\rm long} + T_{\rm short}, \end{aligned} \tag{31}$$

and the definitions are similar in XMM 5. In XMM 6, four flares are observed, with the first being an outlier, and we define

[3]We did not include the Chandra observation on 14 February 2019 in our analysis because the data quality is much lower compared with that in XMM-Newton observations, especially the discontinuous features in the count rates around the background level, which make it hard to pin down the flare starting times. This is attributed to the much smaller effective area of Chandra.

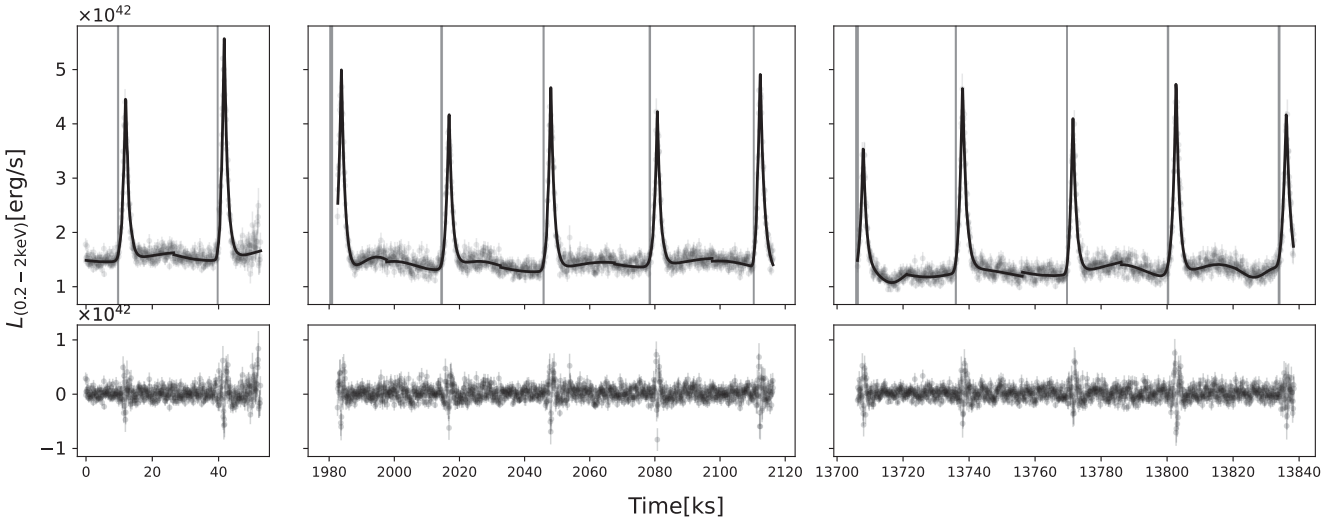

FIG. 3. Same as Fig. 2, but for the phenomenological model.

$$T_{\rm long} = \left(t_0^{(4)} - t_0^{(3)}\right)_{\rm XMM6},$$
$$T_{\rm short} = \left(t_0^{(3)} - t_0^{(2)}\right)_{\rm XMM6},$$
$$T_{\rm sum} = T_{\rm long} + T_{\rm short}. \tag{32}$$

The measured time intervals $P_{\rm QPO}$ and $T_{\rm short,long,sum}$ are consistent with each other, assuming two different light curve models. To quantify the evolution of period $T_{\rm sum}$, we fit the $T_{\rm sum}(t)$ with a linear relation and find that the slope/change rate $\dot{T}_{\rm sum}$ is consistent with zero as

$$\dot{T}_{\rm sum} = \begin{cases} (1.5 \pm 2.6) \times 10^{-5} & \text{plasma ball model} \\ (-4.7 \pm 6.7) \times 10^{-5} & \text{phenomenological model} \end{cases} \tag{33}$$

at the 1-σ confidence level.

TABLE II. Same as Table I, but for the phenomenological model.

Phenomenological model	t_0	$P_{\rm QPO}$	$T_{\rm short}$	$T_{\rm long}$	$T_{\rm sum}$
XMM3 flare 1	662030429^{+104}_{-114}	$51^{+7.50}_{-8.91}$	30025^{+150}_{-158}		
2	662060452^{+78}_{-82}	$52^{+6.80}_{-10.37}$			
XMM4 flare 1	664001278^{+397}_{-326}	$34^{+8.88}_{-8.08}$	31589^{+154}_{-146}	33243^{+236}_{-252}	64842^{+186}_{-210}
2	664035220^{+158}_{-180}	$26^{+1.19}_{-1.03}$			
3	664066491^{+96}_{-97}	$45^{+6.50}_{-4.15}$			
4	664099063^{+136}_{-163}	$50^{+8.15}_{-8.65}$			
5	664130961^{+73}_{-74}	$51^{+7.19}_{-10.46}$			
XMM5 flare 1	675726607^{+357}_{-331}	$18^{+9.23}_{-2.51}$	30258^{+217}_{-215}	33651^{+152}_{-154}	63895^{+221}_{-201}
2	675756547^{+86}_{-95}	$33^{+2.54}_{-1.96}$			
3	675790212^{+81}_{-86}	$55^{+4.96}_{-6.66}$			
4	675820783^{+148}_{-162}	$31^{+1.74}_{-1.43}$			
5	675854426^{+171}_{-191}	$16^{+5.66}_{-2.70}$			
XMM6 flare 1	695049346^{+220}_{-224}	$43^{+1.38}_{-1.22}$	28345^{+983}_{-919}	36847^{+491}_{-505}	65175^{+947}_{-881}
2	695075342^{+790}_{-783}	$18^{+2.27}_{-5.41}$			
3	695103697^{+352}_{-341}	$26^{+1.61}_{-1.34}$			
4	695140539^{+264}_{-262}	$38^{+24.37}_{-25.53}$			
XMM12 flare 1	773633107^{+245}_{-268}	$54^{+5.23}_{-5.05}$	20267^{+300}_{-260}		
2	773653374^{+83}_{-87}	$39^{+13.81}_{-8.84}$			

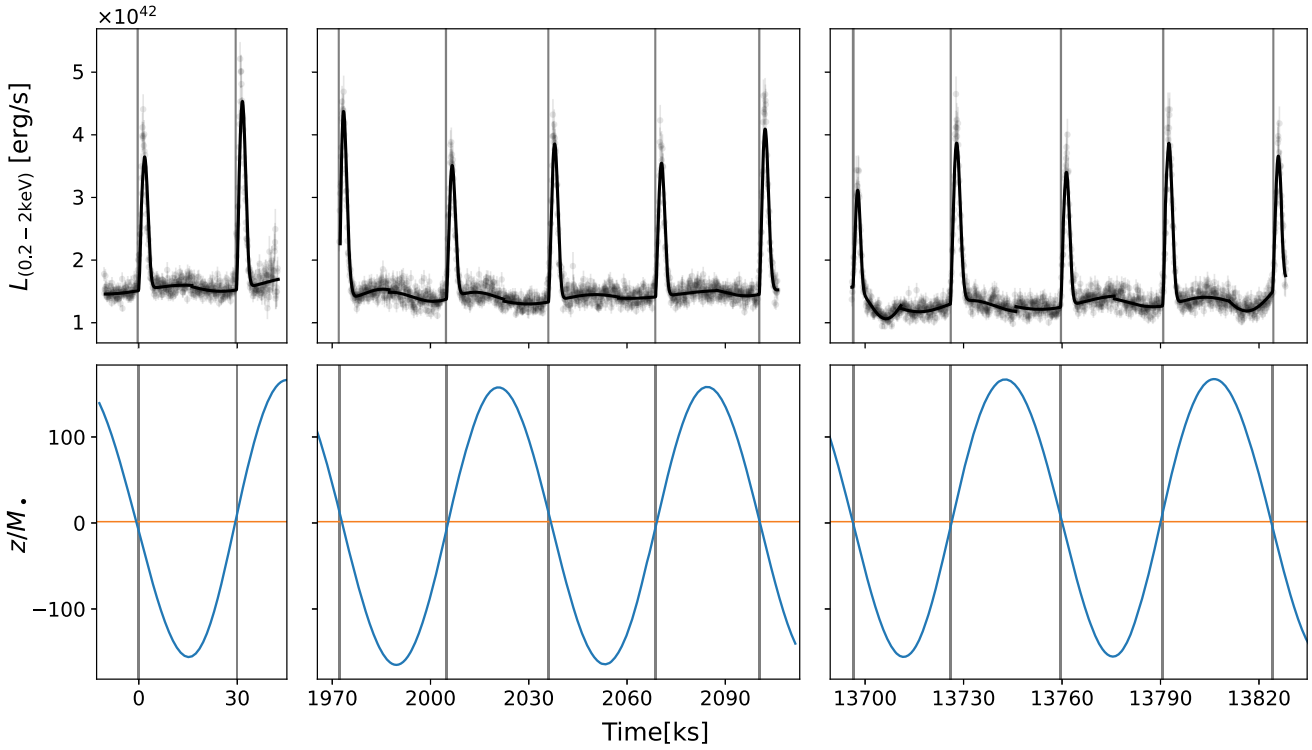

FIG. 4. Top panel: light curve data along with the best fit of the emission model, where the vertical lines are the starting times of the QPEs. Bottom panel: $z(t)$ of the best-fit orbit ($a = 171M_\bullet, e = 0.04, T_{\mathrm{obt}} = 63.7$ ks), where the horizontal line denotes the disk surface $z = H$.

B. EMRI orbital parameters

As explained in the previous subsection, QPEs found in XMM 3–5 are in the regular phase, and we focus on the QPE timing in these three observations for our EMRI orbit analysis (see Sec. IV for more discussions about observations XMM 6 and 12).

In Fig. 4, we show the EMRI orbit of the best-fit flare timing model (with orbital parameters $a = 171M_\bullet, e = 0.04$, $T_{\mathrm{obt}} = 63.7$ ks, and the corresponding SMBH mass $M_\bullet = 1.05 \times 10^6 M_\odot$), along with the starting time t_0 of each flare (Table I). In this model, T_{sum} is simply the orbital period T_{obt} which is a constant if the TDE disk lies on the equator and stays in a steady state as assumed, while the alternating recurrence times are the result of a noncircular orbit plus the different photon propagation times to the observer, and the variation of $T_{\mathrm{long,short}}$ is the result of the SMO orbital precession.

From Fig. 4, we also see that the brighter peak is sometimes associated with the ascending node and sometimes with the descending node of the orbit. The reason for this is that the QPE luminosity is mainly determined by the relative velocity between the SMO and the disk at the collision point as well as the local gas density. From simulations in [40] and the HD simulations shown in Appendix C, the amount of gas bursting out from both sides of the disk after a collision is found to be roughly symmetric; therefore, the collision direction plays a minor role in the QPE luminosity. The collision location and the collision velocity will be modulated on the SMO orbital precession timescale; therefore, the QPE intensities will be modulated on the same timescale as explicitly shown in [33].

The posterior corner plot of all the model parameters is shown in Fig. 10 in Appendix A, where the orbital parameters are constrained as

$$\begin{aligned} a &= 311^{+100}_{-181} M_\bullet, \\ e &= 0.04^{+0.04}_{-0.03}, \\ T_{\mathrm{obt}} &= 63709 \pm 5 \ \ \mathrm{sec}, \end{aligned} \tag{34}$$

at the 2-σ confidence level, respectively. The constraint of the SMBH mass is therefore $M_\bullet \in (2.4 \times 10^5, 1.4 \times 10^6) M_\odot$ at the 2-σ confidence level. In fact, the flare timing contains more information about the SMBH mass than what the simple confidence level shows: There are three peaks in the posterior of the semimajor axis located at $a = \{160, 220, 330\} M_\bullet$, respectively, which correspond to three favored values of the SMBH mass $M_\bullet = \{10^6, 6.2 \times 10^5, 3.4 \times 10^5\} M_\odot$.

For comparison, we performed a similar analysis using the flare starting times $t_0^{(k)}$ in Table II, and the posterior corner plot of the model parameters is shown in Fig. 11,

which is completely consistent with the result shown in Fig. 10.

IV. SUMMARY AND DISCUSSION

In this section, we first summarize different aspects of QPE observations in addition to the recurrence timescales (about a few hours) and the luminosity magnitudes of QPE flares in soft x rays ($\sim 10^{42}$ ergs/s), and we evaluate the performance of the EMRI + TDE disk model in interpreting these observations. Based on the orbital parameters inferred from the flare timing, we then examine which formation channel the EMRI may come from. We conclude this section with a brief discussion about possible ways to distinguish the two and limitations of the flaring time model used in this paper.

A. Observations versus model predictions

A reasonable model must be able to naturally explain, or at least be compatible with, the observations. In the EMRI + TDE disk model, there are two components needed: a TDE disk and a SMO in a proper position. In this subsection, we examine whether the model can naturally explain the QPE observations.

(1) *Alternating long-short occurrence times:* In all the confirmed QPE sources to date with more than three flares detected (GSN 069, eRO-QPE1, eRO-QPE2, and RX J1301.9 + 2747), QPEs have two alternating occurrence times, $T_{\rm long}$ and $T_{\rm short}$ [2–4,34]. In the EMRI + TDE disk model, the secondary SMO crosses the accretion disk twice per orbit, and two different occurrence times $T_{\rm long}$ and $T_{\rm short}$ alternate as a result of the noncircular orbit and different delays of two consecutive collisions [see Eq. (27)].

(2) *Alternating strong-weak QPE intensities:* Strong-weak QPEs alternately occur [2–5,34]. In the EMRI + TDE disk model, the secondary BH crosses the accretion disk twice per orbit, producing two different flares because the two disk crossings are not identical to each other, depending on the orbit eccentricity.

(3) *Spectral evolution:* QPEs measured in higher energy bands are stronger, peak earlier, and have shorter duration than when measured at lower energies [2–5,11,34]. The QPE spectral evolution perfectly matches the flare model prediction where the QPE emission comes from an expanding and cooling plasma ball.

(4) *Light curve profile:* A common feature of QPEs is the fast rise and slow decay light curve profile with a low QPE duty cycle (a few percent) [2–5,34]. Similar to supernova explosions, the thermal radiation from a freely expanding and cooling plasma ball naturally produces the fast rise and slow decay light curve.

(5) *Association with TDEs:* Two QPE sources (GSN 069 and XMMSL1 J024916.6-04124) and a candidate (AT 2019vcb) have been directly associated with x-ray TDEs [5,7–10]. In the EMRI + TDE disk model, two components are needed to produce QPEs: a TDE disk and a SMO in a proper position. Therefore, we do not expect to see QPEs in all TDEs. The fraction depends on the availability of the second component. From the QPEs that are associated with TDEs, we may statistically infer the distribution of SMOs around SMBHs and therefore the EMRI formation rate. In this aspect, QPEs might be a unique probe to EMRIs in the pre-LISA era.

(6) *Association with past AGN activities and not with ongoing AGNs:* The presence of narrow lines in all QPE host galaxies and the absence of luminous broad emission lines indicate that they were recently switched-off AGNs [6,64] (but see also [25] for a different interpretation). In ongoing AGNs, the majority of SMOs in the vicinity of the SMBH are those captured on the AGN accretion disk [65]. As a result, the number of SMOs crossing the AGN disk is suppressed; therefore, there is no QPE association with ongoing AGNs. Past AGN activities are expected to boost the EMRI formation by accelerating the inward migration of SMOs (known as the wet EMRI formation channel [65–68]). In recently turned-off AGNs, SMOs are accumulated on the equator of the SMBH with $a \sim \mathcal{O}(10^2)M_\bullet$ (see [65,66] for the full Fokker-Planck calculation or Sec. IV B for a sketch), while the accretion disk formed from a TDE is, in general, not exactly aligned with the equator; therefore, QPEs are produced as the SMO crossing the TDE formed accretion disk. As we will show in Sec. IV B, the GSN 069 EMRI orbit is consistent with the wet channel prediction while incompatible with alternatives. This adds more independent evidence for the past AGN activities in GSN 069.

(7) *(Anti)association with SMBH mass:* QPEs are preferentially found in nuclei of dwarf galaxies, where the SMBHs are relatively light, with a mass no more than a few times $10^6 M_\odot$ [6,7]. In the EMRI + TDE disk model, this antiassociation with the SMBH mass comes from the TDE rate dependence on the SMBH mass and the finite size of the TDE formed accretion disk. TDEs have been found to be preferentially around lighter SMBHs (see, e.g., Refs. [69,70]). Assuming an α disk of total mass $m_{\rm d}$, we have the disk size

$$r_{\rm d} = 10^2 M_\bullet \left(\frac{m_{\rm d}}{0.35 M_\odot}\frac{\alpha}{0.01}\frac{\dot{M}_\bullet}{0.1\dot{M}_{\bullet,\rm Edd}}\right)^{2/7} \times \left(\frac{M_\bullet}{3\times 10^6 M_\odot}\right)^{-4/7}. \quad (35)$$

For more massive SMBHs, the disk is smaller, and $r_{\rm d}/M_\bullet < 10^2$ for a SMBH heavier than $\sim 3\times 10^6 M_\odot$. The chance of SMOs with $a \sim \mathcal{O}(10^2) M_\bullet$ crossing the TDE formed disk around a more massive SMBH is lower.

(8) *(Anti)association with the SMBH accretion rate in the quiescent state:* Long-term observation of GSN 069 shows that QPEs may only be present below a quiescent luminosity threshold $L_{\rm disk,bol} \sim 0.4 L_{\rm Edd}$ [7]. There are two possible origins of this antiassociation: The ratio of the QPE luminosity to the disk luminosity in the same energy band $L_{\rm QPE}/L_{\rm disk,X}$ depends on the disk accretion rate [33], or QPEs are delayed relative to the TDE by a time interval (which is about a few years in the case of GSN 069).

In the α disk model, the disk surface density $\Sigma \propto \dot{M}_\bullet^{-1}$ and the energy deposited in the SMO-disk collision $\delta E_{\rm SMO} \propto \Sigma$ [Eqs. (2) and (4)] are therefore lower for the higher accretion rate case. The thermal luminosity from the accretion disk $L_{\rm disk,bol} \propto \dot{M}_\bullet$ is higher in the higher accretion case, and the dependence is more sensitive for the soft x-ray luminosity $L_{\rm disk,X}$. As a result, the QPE is harder to identify from the luminous background in the higher accretion rate case (see [33] for the explanation in terms of QPE temperatures and the disk temperature).

The SMO orbit is, in general, not aligned with the TDE disk. The misaligned disk initially precesses like a rigid body before settling down to a nonprecessing warped disk [71–73]. In a recently turned-off AGN, the sBHs are preferentially found on the equator of the SMBH. As a result, the sBH is expected to be highly inclined with respect to the new TDE disk when the sBH-disk collisions are less energetic [Eq. (4)], and QPEs emerge only when the two become nearly aligned and the collisions are sufficiently energetic. This scenario works for sBH EMRIs only, where the emergence of QPEs is delayed by the disk alignment timescale, the accurate value of which is not accurately calculated [74,75].

(9) *Stability:* During the observations XMM 3–5 (regular phase dubbed in [7]), the QPE occurrence times $T_{\rm sum} \coloneqq T_{\rm long} + T_{\rm short}$ are stable with the variation rate $\dot{T}_{\rm sum}$ consistent with zero [see Eq. (33)]. The sBH orbital period change rate due to disk crossing turns out to be [Eq. (4)]

$$\dot{T}_{\rm obt} = \frac{dT_{\rm obt}}{dE_{\rm sBH}}\dot{E}_{\rm sBH} = 3\frac{\delta E_{\rm sBH}}{E_{\rm sBH}} \approx -3\times 10^{-6}\left(\frac{\ln\Lambda}{10}\right) \times \alpha_{0.01}^{-1}\dot{M}_{\bullet,0.1}^{-1} M_{\bullet,6}^{-7/3} T_{\rm obt,20}^{7/3}\left(\frac{m}{30M_\odot}\right)\left(\frac{\sin\iota_{\rm sd}}{0.1}\right)^{-3}, \tag{36}$$

where $T_{\rm obt,20} \coloneqq T_{\rm obt}/20$ hr. The orbital change rate is consistent with the observed $\dot{T}_{\rm sum}$. The star orbital period change rate is given by [76]

$$\dot{T}_{\rm obt} \approx -2\times 10^{-5}\alpha_{0.01}^{-1}\dot{M}_{\bullet,0.1}^{-1} M_{\bullet,6}^{-1} T_{\rm obt,20} m_{\star,\odot}^{-1} \times R_{\star,\odot}^2 \sin\iota_{\rm sd}, \tag{37}$$

where $m_{\star,\odot} \coloneqq m_\star/m_\odot, R_{\star,\odot} \coloneqq R_\star/R_\odot$. The orbital period change rate is also consistent with the current observation constraint.

(10) *Association with QPOs in the quiescent state:* In the old phase (XMM 3–5), quiescent level QPOs were detected with a period close to the corresponding QPE recurrence times $P_{\rm QPO} \in (T_{\rm sum}/4, T_{\rm sum})$ (see Tables I and II), and a 8–10 ks delay with respect to the QPEs [7,11]. It is unclear whether the periodic EMRI impacts on the accretion disk are able to produce the quiescent level QPOs with correct time delay, period, and amplitude.[4]

(11) *New QPE phase in GSN 069:* During the old phase (XMM 3–5), both the QPE intensities and occurrence times alternated with $T_{\rm long} \approx 33$ ks, $T_{\rm short} \approx 31$ ks, and $T_{\rm sum} \approx 64$ ks. During the irregular phase (XMM 6), which is on the rise in TDE 2, the QPE occurrence times observed do not follow the alternating patterns exactly, with the first flare fitting in neither the strong ones nor the weak ones, though flares 2–4 still follow the alternating long-short and strong-weak patterns with $T_{\rm long}^{\rm (irg)} \approx 36$ ks, $T_{\rm short}^{\rm (irg)} \approx 28$ ks, and $T_{\rm sum}^{\rm (irg)} \approx 64$ ks. After disappearing for two years (XMM 7–11), QPEs reappeared (XMM 12) with quite different occurrence times from those in the old phase or the irregular phase: $T_{\rm short}^{\rm (new)} \approx 20$ ks and $T_{\rm long}^{\rm (new)} (> 27\,{\rm ks})$, which are not fully resolved because only two QPEs have been detected [7]. By fitting the variation in the quiescent level with a sine function, the period is constrained to be $P_{\rm QPO}^{\rm (new)} = 54 \pm 4$ ks; however, this period suspiciously coincides with the exposure time, and the statistical quality of the fit is poor, with reduced $\chi_\nu^2 \approx 2.9$ ($\chi^2 = 140$ and $N_{\rm dof} = 49$) [7,11]. This QPO period has been speculated to be same as the QPE period in the new phase, $P_{\rm QPO}^{\rm (new)} \approx T_{\rm sum}^{\rm (new)}$, though this speculated relation was not observed in the previous phases where the QPO periods $P_{\rm QPO}$ were found in the range of $(T_{\rm sum}/4, T_{\rm sum})$ (see Tables I and II). Further measurements with longer

[4]Previous simulations show that the accretion rate $\dot{M}_\bullet$ of the central BH is indeed modulated by periodic stellar-disk collisions [29].

exposure times are needed to confirm whether a different QPE period emerges in the new phase.

In the EMRI + TDE disk model, the shorter $T_{\rm short}^{\rm (new)}$ is a result of a puffier disk due to the higher accretion rate sourced by the TDE 2, and consequently, a larger fraction

$$f_{\rm ebd} \approx \frac{4H/\sin\iota_{\rm sd}}{2\pi r} \approx \frac{1}{3} \times \frac{H}{5M_\bullet} \frac{10^2 M_\bullet}{r} \frac{0.1}{\sin\iota_{\rm sd}} \tag{38}$$

of the EMRI orbit is embedded in the disk. As a result, about $1/3$ of the orbit stays above the disk, which is visible to the observer, making a shorter $T_{\rm short}^{\rm (new)} \approx T_{\rm obt}/3$, and the remaining $\approx 2/3$ is hidden in or below the disk, which is invisible. This geometrical effect of the disk thickness may also contribute to the shorter $T_{\rm short}^{\rm (irg)}$ in XMM 6, which is on the rise in TDE 2.

To identify the true origin(s) of QPEs, all the existing models should be tested against these observations. Taking GSN 069 as an example, the alternating long-short recurrence pattern and a stable $T_{\rm long} + T_{\rm short}$ (see Fig. 1) together pose a huge challenge for the single-period models. In these models, there is no natural explanation without a twofold fine-tuning: alternating delay-advance in the recurrence times for producing the alternating long-short pattern, and cancellation of consecutive delay-advance for producing a stable $T_{\rm sum}$. In the EMRI + TDE disk model, the alternating long-short pattern and the constant $T_{\rm long} + T_{\rm short}$ are natural consequences of a noncircular orbit, and most of the QPE observations summarized above can be quantitatively recovered, though it is unclear whether quiescent-state QPOs can be naturally generated.

In addition to the common properties shared by most QPE sources, GSN 069 is special in the sense that two TDE flares $\sim$9 years apart have been observed. Considering the low TDE rate, the two TDEs are likely two consecutive partial disruptions of the same star. This is similar to another confident repeating partial TDE (pTDE) AT 2020vdq [77], where two consecutive TDEs are found with an interval of $\sim$3 years. The relatively tight orbits are unusual for stars that enter the loss cone driven by two-body relaxation because the TDE rate should be dominated by stars on much wider orbits (see Ref. [78] for a detailed review, and Fig. 5 and the discussion therein for a pictorial understanding). A natural explanation is that the tidally disrupted star comes from a previously tidally disrupted binary (see Refs. [77,79] and Fig. 5).

There are other models where the second TDE flare is due to runaway envelope stripping of the impactor star instead [32]. In this model, there is no need for repeating partial TDEs, and the resumption of QPEs could be due to a surviving stellar core. To distinguish the two models, longer monitoring of GSN 069 and other QPE sources of shorter periods is necessary: (1) After the second flare, a large change in the orbital period is expected in the runaway envelope stripping model; (2) in QPE sources of shorter periods, the second flare should be common because the runaway envelope stripping is more prone to happen.

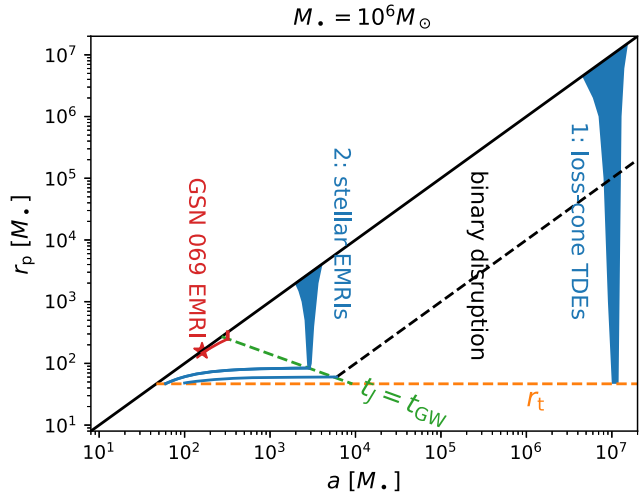

FIG. 5. Following Ref. [28], we use the $r_{\rm p} - a$ phase diagram to analyze the possibility of GSN 069 EMRI formation via the loss-cone channel and the Hills mechanism. As an example, we consider a $10^6 M_\odot$ SMBH and the tidal disruption radius $r_{\rm t} = (M_\bullet/m_\star)^{1/3} R_\star \approx 47 M_\bullet$ of a solar-type star. In the loss-cone channel, there are, in general, two fates of the stars: (1) loss-cone TDEs, most of them being dominated by 2-body scatterings ($t_J < t_{\rm GW}$) and tidal disrupted by the SMBH when scattered into a low-angular momentum orbit with $r_{\rm p} < r_{\rm t}$, and (2) stellar EMRIs, a small fraction of which are scattered into the GW emission dominated regime ($t_J > t_{\rm GW}$), gradually circularizing and losing mass via partial TDEs. Stars residing in a tiny phase space ($r < 300 M_\bullet$ and $e \approx 0$) can possibly become GSN 069-like EMRIs. In the Hills mechanism, the bounded star after a binary disruption is highly eccentric, with eccentricity $e \approx 0.98$ [80] (the black dashed line). The star faces the same two fates, a loss-cone TDE or a stellar EMRI, neither of which ends as GSN 069-like EMRIs.

B. Implications of QPEs on EMRI formation

If QPEs are indeed sourced by impacts of SMOs and accretion disks formed from TDEs, the EMRI orbital parameters will be invaluable for inferring the EMRI formation channels. These SMOs may be captured by the SMBH via the (dry) loss-cone channel [81–86], the Hills mechanism [80,87], or the (wet) AGN disk channel [65–68,88–92]. The EMRI orbits inferred from the six QPE sources have similar properties, with low eccentricity e and pericenter distance $r_{\rm p}/M_\bullet = \mathcal{O}(10^2)$ [32,33]. These orbital parameters are roughly consistent with the (wet) EMRIs formed in AGN disks, where the wet EMRIs are expected to be nearly circular and concentrate around $r = \mathcal{O}(10^2) M_\bullet$ at the end of an AGN phase [65–68], while they are distinct from those EMRIs formed via the loss-cone channel, where

the EMRIs are expected to be highly eccentric ($e \to 1$) and sharply concentrate around $r_{\rm p} = 10M_\bullet$ for sBH EMRIs and around the tidal radius $r_{\rm p} = r_{\rm tidal} = R_\star (M_\bullet/M_\star)^{1/3}$ for stellar EMRIs. A more quantitative analysis for GSN 069 EMRIs is outlined as follows.

In a single-component stellar cluster, the relaxation timescale at radius r due to 2-body scatterings is [93]

$$t_{\rm rlx}(r) = \frac{0.339}{\ln\Lambda}\frac{\sigma^3(r)}{m_\star^2 n_\star(r)}, \tag{39}$$

where $\sigma(r)$ is the local velocity dispersion ($\approx\sqrt{M_\bullet/r}$ within the influence radius $r_{\rm h}$ of the SMBH), $n_\star(r)$ is the star number density, and $\ln\Lambda \approx 10$ is the Coulomb logarithm. Using the empirical $M_\bullet - \sigma_\star$ relation [94,95], the influence radius $r_{\rm h} \coloneqq M_\bullet/\sigma_\star^2$ turns out to be

$$r_{\rm h} \approx M_{\bullet,6}^{0.5}\ {\rm pc}. \tag{40}$$

For a highly eccentric orbit, the angular momentum only needs to change slightly to make an order unity difference in the orbit, and the diffusion timescale in the angular momentum, in general, is shorter than the relaxation timescale in the energy as $t_J \approx (1-e^2)t_{\rm rlx}$. For comparison, the energy dissipation timescale of the star due to GW emission is [96]

$$t_{\rm GW} = -\frac{a}{\dot a} \approx \frac{a^4}{M_\bullet^2 m_\star}\left(\frac{r_{\rm p}}{a}\right)^{7/2}, \tag{41}$$

where $r_{\rm p} = a(1-e)$ is the pericenter distance. Assuming the Bahcall-Wolf (BW) density profile $n_\star(r) \propto r^{-7/4}$ [97], one can find the ratio [28]

$$\frac{t_J}{t_{\rm GW}} \approx \left(\frac{r_{\rm p}}{M_\bullet}\right)^{-5/2}\left(\frac{a}{r_{\rm h}}\right)^{-5/4}. \tag{42}$$

To analyze the formation rate of GSN 069-like EMRIs in the loss-cone channel, a $r_{\rm p} - a$ diagram proposed in Ref. [28] is useful. As shown in Fig. 5, most stars are dominated by 2-body scatterings and become tidally disrupted when scattered into a low-angular momentum orbit with $r_{\rm p} < r_{\rm t}$; a small fraction of stars are scattered into the GW emission dominated regime (dubbed as stellar EMRIs), gradually circularizing and finally losing mass via partial TDEs. The GSN 069 EMRI is one of the stellar EMRIs. The TDE rate and stellar EMRI formation rate can be estimated as

$$R_\star(<r) \approx \frac{N_\star(<r)}{t_{\rm rlx}(r)} \propto r, \tag{43}$$

from which we find the ratio of the formation rate of GSN 069-like EMRIs (EMRIs with orbital parameters $e < 0.1$ and $T_{\rm obt} > 63$ ks that are confidently consistent with that of the GSN 069 EMRI and, of course, in the GW emission dominated regime with $t_J > t_{\rm GW}$) to the total TDE rate as

$$\frac{R_\star(<300M_\bullet)}{R_\star(<r_{\rm h})} \approx 10^{-5}, \tag{44}$$

where we have used the fact that only stars in the range of $r < 300M_\bullet, e \approx 0$ can possibly become GSN 069-like EMRIs (see Fig. 5). The ratio becomes even lower if we consider the mass-segregation effect where the star density is expected to be suppressed at small radii [81–86]. Therefore, the stellar EMRI in GSN 069 unlikely comes from the loss-cone channel, and a similar analysis also applies to sBH EMRIs.

The Hills mechanism has been proposed as an efficient EMRI formation channel, and the sBH EMRIs at coalescence from this channel were speculated to be nearly circular due to the long inspiral phase [80]. However, recent simulations that take the mass segregation effect into account show that the orbital eccentricity of sBH EMRIs at coalescence actually peaks at high eccentricity, following a distribution similar to in the loss-cone channel [87]. For EMRIs in the earlier inspiral phase with orbital semimajor axis $a = \mathcal{O}(10^2 M_\bullet)$, the orbital eccentricity should be even higher, which is in contrast with low-eccentricity EMRI in GSN 069. From Fig. 5, the same conclusion can be obtained. In the Hills mechanism, the bounded stars after binary disruptions are highly eccentric, with eccentricity $e \approx 0.98$ [80]. The stars face the same two fates, and neither of them ends as GSN 069-like EMRIs: Most stars end as loss-cone TDEs, and the remaining small fractions of stars evolve into stellar EMRIs; however, they are too eccentric to become GSN 069-like EMRIs. A similar analysis also applies to sBH EMRIs.

In the wet EMRI formation channel, a SMO orbiting around an accreting SMBH can be captured by the accretion disk as interactions (dynamical friction and density waves) with the accretion disk tend to decrease to the orbital inclination angle with respect to the disk. After captured on the disk, the SMO migrates inward, driven by the density waves and gravitational wave emission. The orbital eccentricity is expected to be damped by the density waves to $e \sim h$, where h is the disk aspect ratio. The number $N_{\rm SMO}(<r)$ of SMO captured is determined by

$$\frac{\partial}{\partial t}N_{\rm SMO} + \frac{\partial}{\partial \ln r}\left(N_{\rm SMO}\frac{v_{r,\rm mig}}{r}\right) = F_{\rm cap}(r), \tag{45}$$

where $F_{\rm cap}(r)$ is the capture rate of SMOs from the nuclear stellar cluster and $v_{r,\rm mig}$ is the migration velocity in the radial direction. The migration is dominated by the GW emission at small separations and by the type-I migration at large separations [67], $v_{r,\rm mig} = v_{r,\rm GW} + v_{r,\rm I}$, with

$$v_{r,\rm GW} = -\frac{64}{5}\frac{mM_\bullet^2}{r^3} \tag{46}$$

and

$$v_{r,\mathrm{I}} = -(2.7 + 1.1\alpha_s)\frac{m\Sigma r^3\Omega}{M_\bullet^2 h^2}, \tag{47}$$

where $\alpha_s \coloneqq d\ln\Sigma/d\ln r$, $\Omega(r)$ is the disk angular velocity, and $h(r)$ is the disk aspect ratio [98,99]. To obtain the SMO number $N_{\mathrm{SMO}}(<r)$, SMOs captured by the disk (disk component) and those residing in the cluster (cluster component) should be evolved self-consistently (see, e.g., Refs. [65–68]). Here, we focus on the distribution of disk-component SMOs in the vicinity of a SMBH ($r < 10^3 M_\bullet$), where the capture rate is negligible and the distribution is clearly $N_{\mathrm{SMO}} \propto r/v_{r,\mathrm{mig}}$, in a steady state. As a result, we obtain $N_{\mathrm{SMO}} \propto r^4$ in the GW emission dominated regime and $N_{\mathrm{SMO}} \propto r^{-4}$ in the type-I migration dominated regime for an α disk. In Fig. 6, we show the distributions $dN_{\mathrm{SMO}}/d\ln r$ for a few AGN examples, where $dN_{\mathrm{SMO}}/d\ln r$, in general, peaks at $r = \mathcal{O}(10^2 M_\bullet)$ for SMBHs with masses in the range of $10^{5-7} M_\odot$. After the AGN turns off, the SMOs will migrate inward, driven solely by GW emissions, and the distribution of SMOs in the radial direction will be reshaped, with the peak moving outwards to a larger radius. Therefore, the EMRI in GSN 069 is consistent with the wet channel expectation.

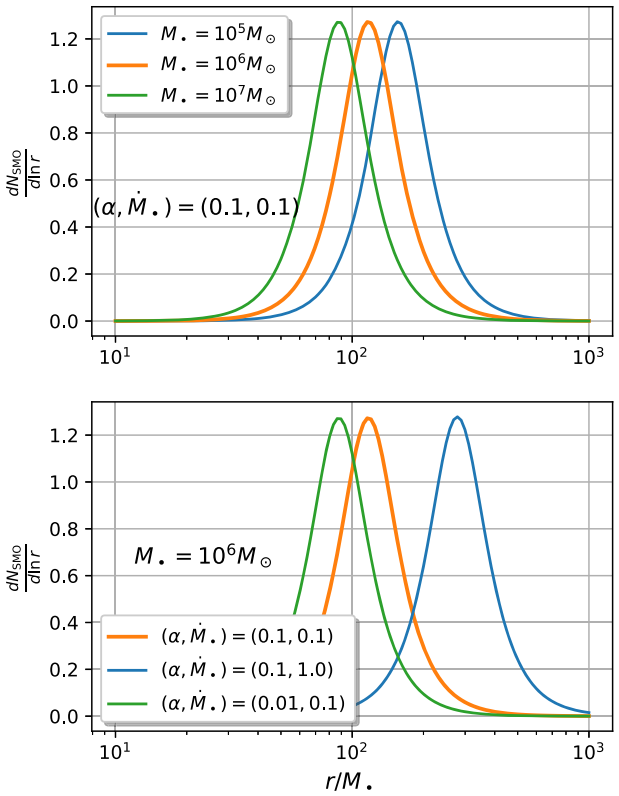

FIG. 6. Distribution $\frac{dN_{\mathrm{SMO}}}{d\ln r}$ of SMOs that are captured on an AGN disk, where we have normalized the total number N_{SMO} to be unity. Stars follow the same distribution if they are not destroyed in collisions with the AGN disk and with other stars or sBHs. The AGN disk is modeled as an α disk with viscosity parameter α and accretion rate $\dot{M}_\bullet$ (in units of $\dot{M}_{\bullet,\mathrm{Edd}}$).

In the above analysis, we did not take the tidal circularization process of the stellar orbit into account, which turns out to be subdominant. As shown in Ref. [100], the tidal circularization rate of the stellar orbit around a SMBH is

$$\begin{aligned}\left.\frac{d\ln e}{dt}\right|_{\mathrm{tide}} &\approx -0.09 T_{\mathrm{eff},5800}^{4/3} M_{\mathrm{env},0.02}^{2/3} M_{\star,\odot}^{-1}\left(\frac{M_\bullet}{M_\star}\right)^2\left(\frac{R_\star}{a}\right)^8 \mathrm{yr}^{-1}\\ &\approx 5\times 10^{-10} T_{\mathrm{eff},5800}^{4/3} M_{\mathrm{env},0.02}^{2/3}\\ &\quad\times\left(\frac{T_{\mathrm{obt}}}{64\ \mathrm{ks}}\right)^{-16/3} M_{\bullet,6}^{-2/3} M_{\star,\odot}^{-3} R_{\star,\odot}^{8}\ \mathrm{yr}^{-1},\end{aligned} \tag{48}$$

where M_{env} is the mass of the stellar convective envelope and T_{eff} is the stellar effective temperature. In comparison with the circularization rate driven by GW emission [96],

$$\begin{aligned}\left.\frac{d\ln e}{dt}\right|_{\mathrm{GW}} &= -\frac{304}{15}\frac{M_\bullet^2 M_\star}{a^4} g(e)\\ &\approx -2\times 10^{-7} g(e)\left(\frac{T_{\mathrm{obt}}}{64\ \mathrm{ks}}\right)^{-8/3} M_{\bullet,6}^{2/3} M_{\star,\odot}\ \mathrm{yr}^{-1},\end{aligned} \tag{49}$$

where

$$g(e) = (1-e^2)^{-5/2}\left(1 + \frac{121}{304}e^2\right), \tag{50}$$

we find

$$\begin{aligned}\frac{\dot{e}|_{\mathrm{GW}}}{\dot{e}|_{\mathrm{tide}}} &\approx 400 T_{\mathrm{eff},5800}^{-4/3} M_{\mathrm{env},0.02}^{-2/3}\left(\frac{T_{\mathrm{obt}}}{64\ \mathrm{ks}}\right)^{8/3}\\ &\quad\times M_{\bullet,6}^{4/3} R_{\star,\odot}^{-8} M_{\star,\odot}^{4} g(e).\end{aligned} \tag{51}$$

Therefore, the tidal circularization was never dominant compared with the GW emission, and it can be safely ignored.

For the SMO settling down to a low-eccentricity orbit around the central SMBH, Kozai-Lidov oscillations driven by a third body must be quenched, e.g., by the apsidal precession of the SMO. The quench condition that the precession period is shorter than the Kozai-Lidov oscillation period $P_{\mathrm{pre}} < P_{\mathrm{K-L}}$ has been derived as [101]

$$\frac{a_3^3}{a^3} > \frac{3m_3 a(1-e_3^2)^{3/2}}{4M_\bullet^2(1-e^2)^{3/2}}, \tag{52}$$

where m_3, a_3, and e_3 are the mass, the semimajor axis, and the orbital eccentricity of the third body. For the EMRI system in GSN 069 with $a = \mathcal{O}(10^2)M_\bullet$, the above

condition is guaranteed as long as $m_3 \lesssim M_\bullet$ (and of course $a_3 > a$). As shown in Ref. [102], the maximum orbital eccentricity that could be excited turns out to be $e_{\max} \approx \sqrt{P_{\rm pre}/P_{\rm K-L}} \ll 1$, assuming an initial circular orbit and a stellar mass third object $m_3 \lesssim 10^2 M_\odot$. Therefore, Kozai-Lidov oscillations are not expected to drive the SMO off the low-eccentricity orbit.

To summarize, the low-eccentricity EMRI with semi-major axis $a = \mathcal{O}(10^2) M_\bullet$ [Eq. (34)] in GSN 069 seems unlikely to be from the loss-cone channel or the Hills mechanism, and it is consistent with the wet EMRI channel prediction. In Fig. 7, we tentatively display the whole history of GSN 069 EMRI formation in a previous AGN phase and the ongoing QPEs from EMRI and TDE disk collisions.

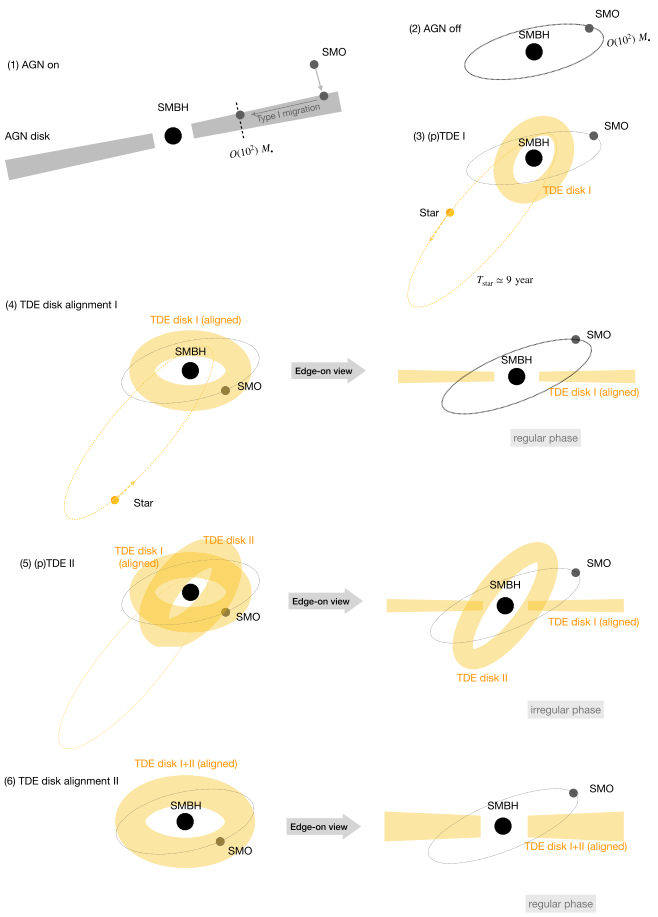

FIG. 7. Cartoon plot showing the whole history of GSN 069 EMRI formation and QPE production. (1) In a previous AGN phase, a SMO is captured on the AGN disk and migrates inward, driven by density waves, until $r = O(10^2) M_\bullet$, where GW radiation takes over; (2) after the AGN turns off, the SMO resides on a nearly circular orbit with radius $r = O(10^2) M_\bullet$; (3) a star is partially tidally disrupted, and the stripped gas forms a TDE disk later; (4) the regular phase of QPEs starts when the gas settles down into a TDE disk, which takes a few years to be aligned on the equator; (5) the regular QPE phase is disturbed by the second tidal disruption of the star; (6) a new regular QPE phase starts after the gas from the second (p)TDE settles down.

C. sBH EMRIs versus stellar EMRIs

In the EMRI + TDE disk model, the secondary object could be a normal star [32] or a sBH [33], which can predict similar QPE properties and are not easy to be distinguished from current QPE observations (see the above two references for more detailed arguments). Identifying the nature of the secondary object will be invaluable for accurately predicting the rate of EMRIs detectable by spaceborne GW detectors and for distinguishing different accretion disk models in light of the increasing number of QPE detections.

Both models predict a decay in the orbital period due to energy loss in the collisions with different rates $\dot{T}_{\rm obt}$ [see Eqs. (36) and (37)]. The current constraint is not sufficiently accurate for distinguishing the two [see Eq. (33)]. Longer monitoring of the existing QPE sources is necessary to pin down the orbital period decay rate $\dot{T}_{\rm ob}$ and, consequently, identify the nature of the SMO.

In the two models, the lifetime of QPE activities might be different. In general, three timescales are relevant to the QPE lifetime [32,33]: the SMO orbital decay timescale $t_{\rm decay}$, the TDE disk lifetime $t_{\rm TDE\ disk}$, and the star survival timescale $t_{\star,\rm sur}$ (for stellar EMRIs only). The decay timescale $t_{\rm decay} := |T_{\rm obt}/\dot{T}_{\rm obt}| = \mathcal{O}(10^3\text{–}10^4)$ yr [Eqs. (36) and (37)] is much longer than $t_{\rm TDE\ disk} = \mathcal{O}(1\text{–}10)$ yr. The star survival timescale interacting with the TDE disk is rather uncertain. In Ref. [32], $t_{\star,\rm sur}$ is estimated as the star mass ablation timescale,

$$t_{\star,\rm sur} := \frac{m_\star}{\Delta m_\star}\frac{T_{\rm obt}}{2} \approx 160\alpha_{0.01} M_{\bullet,6}^{4/3} \dot{M}_{\bullet,0.1}^{2} T_{\rm obt,20}^{2/3} m_{\star,\odot}^{2} R_{\star,\odot}^{-4}\ {\rm yr}, \quad (53)$$

within which the star loses most of its mass as it crosses the TDE disk, and a small amount of gas $\Delta m_\star$ gets stripped away each time due to the ram pressure. In this estimate, the star survives sufficiently long, and the lifetime of QPE activities will be roughly $t_{\rm TDE,disk}$. In Ref. [33], $t_{\star,\rm sur}$ is estimated by comparing the impact energy $\delta E_\star$ with the star binding energy $E_{\rm bind} := G m_\star^2/2R_\star$,

$$t_{\star,\rm sur} := \frac{E_{\rm bind}}{\delta E_\star}\frac{T_{\rm obt}}{2} \approx 12\alpha_{0.01}\dot{M}_{\bullet,0.1} M_{\bullet,6}^{1/3} T_{\rm obt,20}^{2/3} (\sin\iota_{\rm sd})^{-1} m_{\star,\odot}^{2} R_{\star,\odot}^{-3}\ {\rm d}. \quad (54)$$

This estimate gives a much shorter star survival time and disfavors the stellar EMRI model. Therefore, the lifetime of QPE activity is roughly equal to the TDE disk lifetime $\mathcal{O}(1\text{–}10)$ yr in the sBH EMRI model, while it is much more uncertain in the stellar EMRI model due to the uncertain star survival time. Detailed simulations of star-disk

collisions are necessary for figuring out the star survival time. Once confirmed, the lifetime of QPE activities will be useful in distinguishing the two models.

Both models predict the strong-weak pattern in the QPE intensities, though with different dependence on the orbital eccentricity: $\delta E_{\rm sBH} \propto \Sigma r \propto r^{5/2}$ and $\delta E_\star \propto \Sigma r^{-1} \propto r^{1/2}$ from Eqs. (2) and (4). Therefore, the strong-weak QPE intensity contrasts are $(I_{\rm strong}/I_{\rm weak} - 1) \leq (r_{\rm a}/r_{\rm p} - 1)^{5/2{\rm or}1/2} \approx 5e$ or e in these two models, respectively. For GSN 069, the intensity contrasts are roughly 30% (see Fig. 1), requiring an orbital eccentricity $e \approx 0.06$ for the sBH EMRI and $e \approx 0.3$ for the stellar EMRI. The EMRI orbital eccentricity obtained from the QPE timing is $e = 0.04^{+0.04}_{-0.03}$ at the 2-σ confidence level, which favors the sBH EMRI. However, this inference depends on the standard α disk assumption, with the disk surface density $\Sigma \propto r^{3/2}$, the accuracy of which is not yet confirmed for TDE disks. For example, in the β disk model where $\Sigma \propto r^{-8/5}$ [42], the conclusion will be the opposite. An important consequence of this dependence on the disk surface density profile is that the QPEs can be used as a probe to different accretion disk models as long as the nature of the SMO is confirmed, say, via the orbital change rate $\dot{T}_{\rm obt}$ or the star survival time $t_{\star,{\rm sur}}$ as explained in the previous paragraphs.

In the above intensity analysis, we have implicitly assumed the symmetry of the emissions about the midplane of the disk after being shocked by the SMO from either direction, i.e., $I^{\uparrow\gamma}_{\downarrow v} = I^{\downarrow\gamma}_{\downarrow v}$ and $I^{\uparrow\gamma}_{\uparrow v} = I^{\downarrow\gamma}_{\uparrow v}$, where $\updownarrow v$ denote the SMO moving directions and the $\updownarrow\gamma$ denote the emission directions. The (approximate) symmetry has been verified in local simulations of sBH-disk collision [40] but may not be true for star-disk collisions, where the emission could be preferably on one side of the post-collision disk due to the large geometrical size of the star. Such kinds of asymmetry are indeed observed in our global HD simulations with different geometrical sizes of SMO colliding with the disk (see Appendix C for more details). Specifically, with a large softening/sink particle radius to mimic the star-disk collision, the integrated density and temperature perturbations from the lower and upper disks behave more asymmetrically than the smaller softening case. However, this kind of asymmetry is not as strong as we expect. We suspect that this could be due to the fact that we have not explored the extremely large geometry size contrast for these two scenarios, which is unlikely feasible in our global HD simulations.

In the above intensity analysis, we have also assumed a steady axisymmetric accretion disk. In fact, the TDE disk might be lopsided or eccentric [103]. Though the nonaxisymmetric nature of the disk does not change the alternating strong-weak pattern in the QPE intensities, it is expected to modulate the QPE intensities on the SMO orbital precession timescale as the collision positions vary.

D. Model imitations and future work

In this work, we have focused on the analysis of the QPE source GSN 069. In principle, one can conduct a full parameter inference on the EMRI orbital model and the flare emission model. In fact, it is not straightforward to accurately model the QPE light curves with simple emission models. In this work, we used an expanding plasma ball model and a phenomenological model, both of which might be subject to some systematics in determining the flare starting times $t_0^{(k)} \pm \sigma(t_0^{(k)})$ (see discussion about identifying possible systematics from HD simulations in Appendix C). To mitigate the impact of these potential systematics, we multiply the uncertainties by a scale factor F_t in inferring the EMRI orbital parameters from the flare starting times. Another degree of freedom we did not consider in this work is the SMBH spin, which drives Lense-Thirring precession and consequently modulates the QPE recurrence times.

We will improve these model limitations and apply the improved analysis on all the existing QPE sources in a follow-up work, where the SMBH spin is straightforward to take into consideration in the EMRI orbits. The emission model systematics may be improved with a simulation motivated model and/or a hierarchical inference method [104] widely used in the GW community.

Recently, QPEs with recurrence times of ~3 weeks were found in the source Swift J0230 + 28 [105,106], and it is interesting to see whether these QPEs fit in the same framework.

ACKNOWLEDGMENTS

We thank the referee for carefully reading this paper and providing encouraging and valuable comments. We thank Liang Dai, Dong Lai, and Bin Liu for enlightening discussions. We also thank Jialai Kang, Shifeng Huang, and Giovanni Miniutti for helpful discussions on the x-ray data analysis and Qian Hu for valuable discussions. L. H. acknowledges support from the National Natural Science Foundation of China (Grants No. 11933007 and No. 12325302), the Key Research Program of Frontier Sciences, CAS (Grant No. ZDBS-LY-SLH011), and the Shanghai Pilot Program for Basic Research-Chinese Academy of Science, Shanghai Branch (Grant No. JCYJ-SHFY-2021-013). Y. P. L. is supported in part by the Natural Science Foundation of China (Grants No. 12373070 and No. 12192223) and the Natural Science Foundation of Shanghai (Grant No. 23ZR1473700). This work has been supported by the National Key R&D Program of China (No. 2022YFA1603104), and Key Research Program of Frontier Sciences, CAS (Grant No. QYZDJ-SSW-SLH057). The calculations have made use of the High Performance Computing Resource in the Core Facility for Advanced Research Computing at the Shanghai Astronomical Observatory. This paper used data from XMM-Newton, an ESA science mission with instruments and contributions directly funded by the ESA Member States and NASA.

APPENDIX A: CONSTRAINTS ON THE PARAMETERS OF THE EMISSION MODEL AND THE FLARE TIMING MODEL

Figure 8 displays the posterior corner plot of the plasma ball model parameters for the second flare in XMM 5. In Fig. 9, we show the evolution of the plasma ball size $R(t)$ and the effective temperature $T_{\rm eff}(t)$, and its spectral evolution in the best-fit model of the second flare in XMM5. Around the peak of the QPE luminosity, the plasma ball effective temperature is ≈0.5 keV, which is higher than the observed value by a factor of 2–3, though the uncertainty in the initial temperature is large (see Fig. 8). This tension implies the limitation of the simple expanding plasma ball emission model. This is one of the reasons we consider an alternative phenomenological model for fitting the QPE light curves.

Figure 10 displays the posterior corner plot of the EMRI orbital parameter constrained by the flare starting times $t_0^{(k)}$

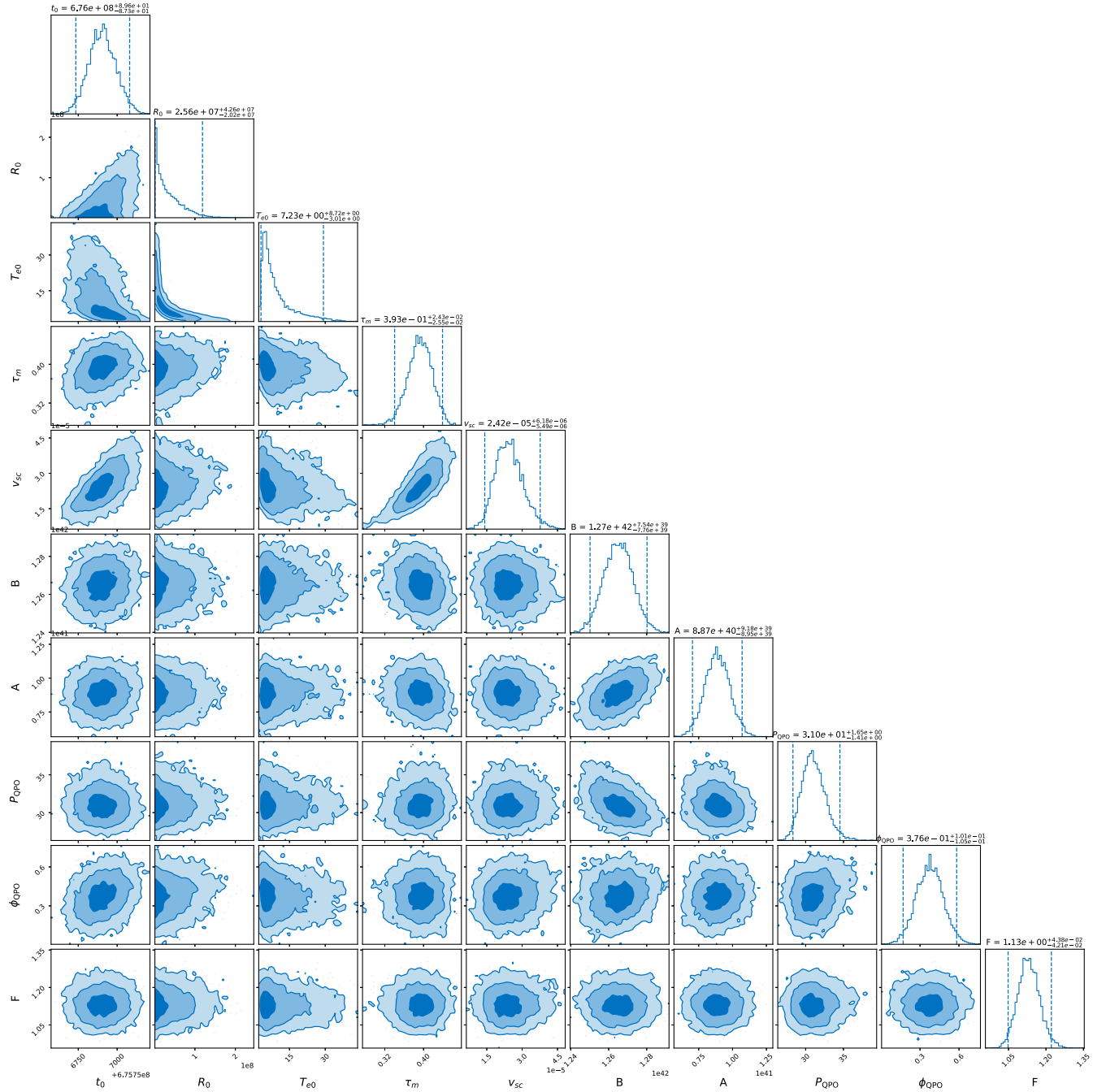

FIG. 8. Corner plot of the emission model parameters of the second flare in XMM5: t_0[sec], R_0[cm], T_{e0}[keV], τ_m[hour], v_{sc}[c], B[erg/s], A[erg/s], $P_{\rm QPO}$[ks], $\phi_{\rm QPO}$, F, where each pair of vertical lines denotes the 2-σ confidence level.

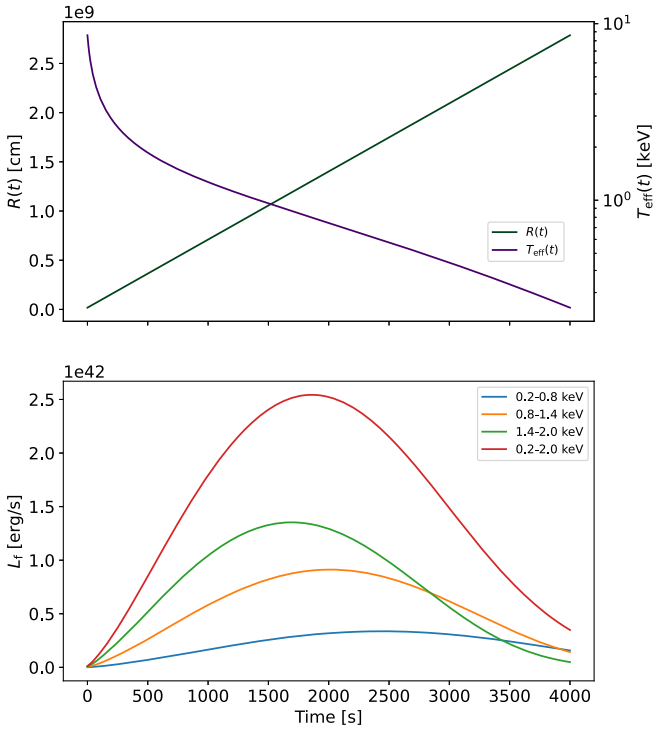

FIG. 9. Details of the best-fit model of the second flare in XMM5. Top panel: evolution of the plasma ball radius and effective temperature, $R(t), T_{\rm eff}(t)$. Bottom panel: spectral evolution of the plasma ball emission, where eruptions measured in higher energy bands are stronger, peak earlier, and have shorter duration than when measured at lower energies.

shown in Table I. All the angles defining the orbital plane orientation and the LOS direction are not well constrained saturating their priors, but the posteriors of the intrinsic orbital parameters yield important clues about the EMRI formation history as explained in Sec. IV.

APPENDIX B: SCATTER EXPERIMENTS OF THE REMNANT STAR AND SMO

If the new period $T_{\rm sum}^{\rm (new)}$ in XMM 12 turns out to be largely different from those in the old regular phase and in the irregular phase, this new phase will pose a challenge to many existing models, including the EMRI + TDE disk model. There was some speculation that the shorter $T_{\rm short}^{\rm (new)}$ and $T_{\rm sum}^{\rm (new)}$ are the result of a large change in the EMRI orbital ($\sim$10% decrease in the semimajor axis and $\sim$0.2 increase in the eccentricity) after a close encounter with the remnant star at its pericenter during TDE 2. We examine this speculation using scattering experiments, and we find that such a large orbital change seems unlikely.

In order to test whether the orbital eccentricity of the SMO can be excited during the close encounter with the remnant star, we perform scatter experiments with N-body simulations to follow the orbital evolution of the sBH or the star during and after the TDE 2 event.

We use a fourth order Hermite integrator with a block time step [107] to calculate the orbital evolution of the two bodies. We first consider the case where a remnant star that has experienced TDE 1 and a sBH are orbiting a SMBH. The masses of the remnant star, the sBH, and the SMBH are set to $2.5M_\odot$, $10M_\odot$, and $10^6M_\odot$, respectively. The remnant star has a pericenter distance of $100M_\bullet$ and an orbital period of 9 years, which yields an eccentricity of 0.9954. The orbital inclination of the star is set to 0. The sBH has an initially low eccentricity of 0.05 and a semimajor axis of $160M_\bullet$. The orbital inclination of the sBH is randomly chosen from 0 to π. The other orbital elements (the longitude of the ascending node, the argument of the pericenter, and the time of the pericenter passage) are randomly chosen from 0 to 2π. We also consider the case where the remnant star encounters another star instead of a sBH near the pericenter. In this case, the sBH is replaced by a star of $1M_\odot$. The orbital parameters remain unchanged.

In both cases, we integrate the system for roughly half an orbit of the remnant star to capture the orbital change of the SMO before and after the close encounter with the remnant star at the pericenter. A softening parameter $\epsilon \simeq 2R_\odot$ is used for the close encounter. In each case, 1000 simulations are performed. No close encounters lead to a 10% decrease in the orbital semimajor axis or a 0.2 increase in the orbital eccentricity.

APPENDIX C: HD SIMULATIONS OF SMO-DISK OSCILLATIONS

We carry out a few 3D hydrodynamical simulations for the SMO-disk collision using Athena++ [108]. The thin disk is initialized with an aspect ratio of $h/r = 0.03$, and an α viscosity [41] is implement with $\alpha = 0.1$. For simplicity, the SMO collides vertically with the disk around the central SMBH. The SMO is initially far above the midplane such that the gravitational interaction between the SMO and the disk is weak. The motion of the SMO is prescribed by only the vertical velocity $-v_{\rm k}$ while fixing cylindrical $R = r_0$ and azimuthal $\phi = 0$ locations in time, where $v_{\rm k}$ is the local Keplerian velocity.

The gravitational potential of the SMO is softened with the classical Plume potential, with a softening scale of ϵ, and the accretion of the SMO is modeled as a sink particle with the same softening radius ϵ. The softening/sink radius mimics the physical size of the SMO. We adopt different softening/sink radii ($\epsilon = 0.1\,R_{\rm H}$ and $\epsilon = 0.3\,R_{\rm H}$) to quantify the effect of the different physical size of the SMO on the collision-induced emission, where $R_{\rm H}$ is the Hill radius of the colliding object. With a mass ratio of $q = 10^{-3}$ and $R_{\rm H} = 0.07r_0$, this leads to $\epsilon = 0.007r_0$ and $\epsilon = 0.02r_0$, respectively. A relatively large mass SMO is adopted to save the computational cost, as it is very challenging to well resolve the sink radius of the realistic mass ratio object even with grid refinement, e.g., $q \lesssim 10^{-5}$. The softening scale

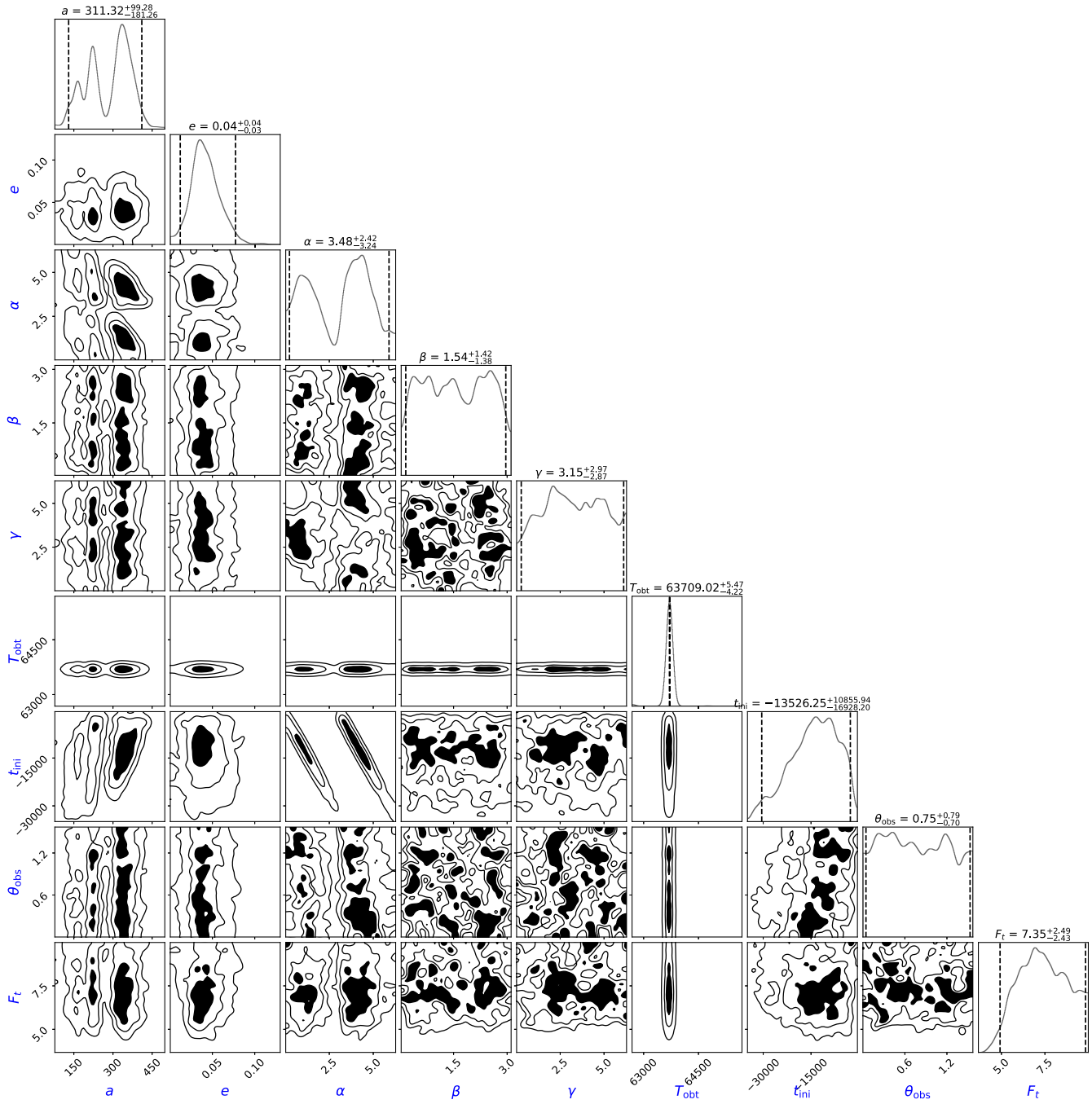

FIG. 10. Posterior corner plot of the flare timing model parameters: $a[M_\bullet], e, \alpha, \beta, \gamma, T_{\rm obt}[\rm sec], t_{\rm ini}[\rm sec], \theta_{\rm obs}, F_t$, where each pair of vertical lines denotes the 2-σ confidence level. The data used are the flare starting times $t_0^{(k)}$ shown in Table I.

adopted here is still too large compared to the size of the sBH, which is way too small to simulate numerically. For stellar-mass black hole collision, the sink hole radius could be as small as the event horizon of the sBH and orders of magnitude smaller than the Bondi/Hill radius of sBH. The case with a larger softening size is adopted for the case of star-disk collision, for which the physical size of the star is usually much larger than the Bondi radius.

We evolve the gas adiabatically, with an adiabatic index $\gamma = 4/3$. The disk is resolved with a root grid of $[n_r, n_\theta, n_\phi] = [128, 16, 512]$, where the radial domain is $[0.5, 2.5]r_0$, and a 3.5 disk scale height is modeled in the θ direction. Three levels of static refinement with a refine sphere of $\delta r = 0.07 r_0$ around the midplane are adopted to well resolve the collision location. As such, we can well resolve the Hill radius of the SMO with 40 grids in each dimension.

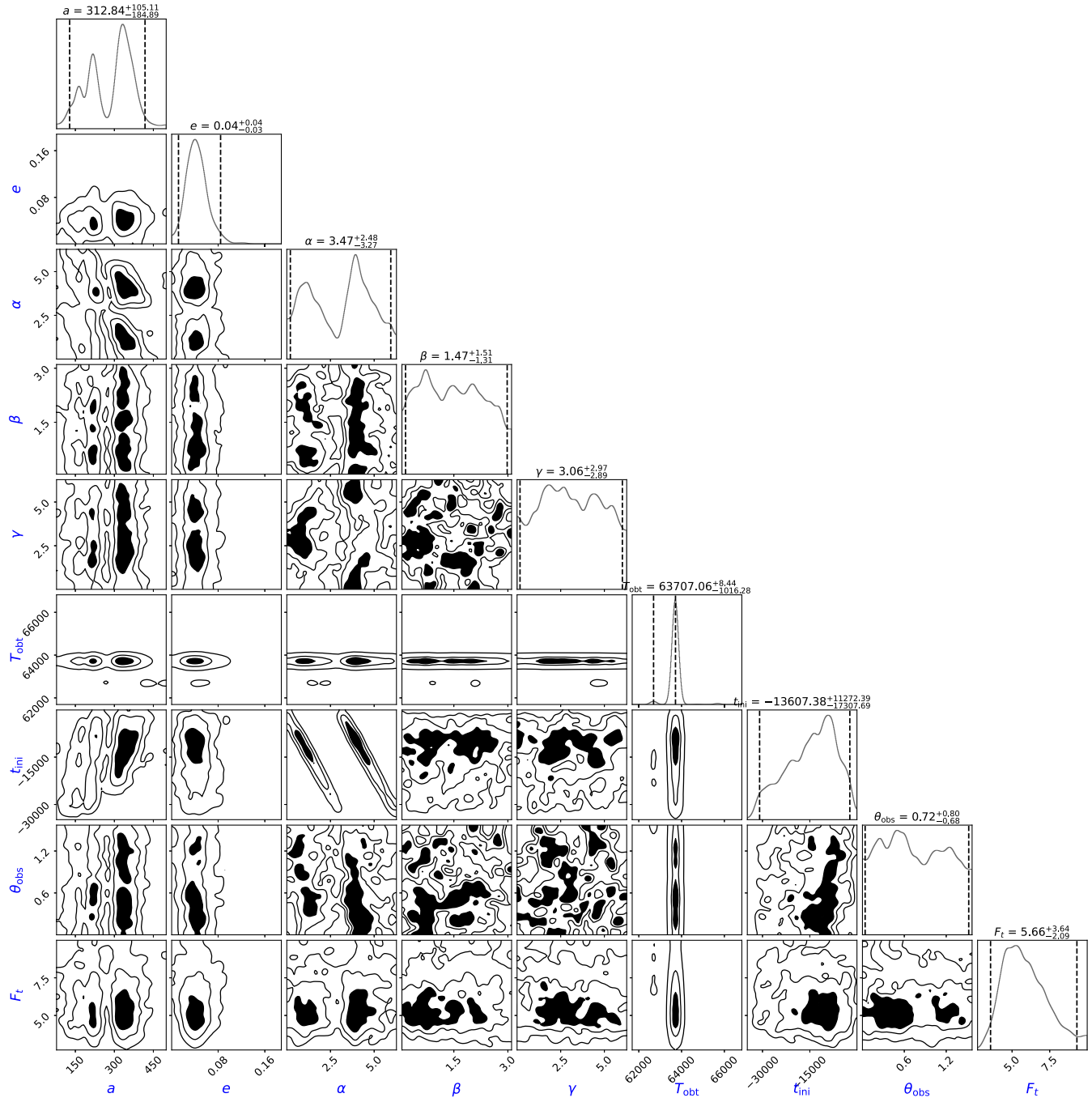

FIG. 11. Similar to Fig. 10, except the data used are the flare starting times $t_0^{(k)}$ in Table II.

After the SMO-disk collision, there exists strong shocks which heat the gas around a narrow band of the collision site. By checking the vertical density and pressure distribution as shown in Figs. 12 and 13, the postcollision perturbation is asymmetric above and below the disk midplane. There is a dense blob above the midplane before $t = 0.5$, i.e., prior to the collision at the midplane. The hot blob expands radially and vertically, suffering from shearing motion of the disk, which can induce spiral arms in the disk. The perturbation then becomes stronger at the lower half plane of the disk, i.e., after the collision at the midplane. This asymmetric pattern is slightly stronger for the star-disk collision with a larger ϵ (at time $t = 0.6$ of Figs. 12 and 13).

The shocked-heated dense blob will be responsible for the x-ray emission in observations. To quantify the emission features, we calculate the perturbed disk mass around the collision site $r = [0.8, 1.2]r_0$, and we integrate the disk mass from the upper and lower halves of the disk for two different softening/sink radii, shown in Fig. 14.

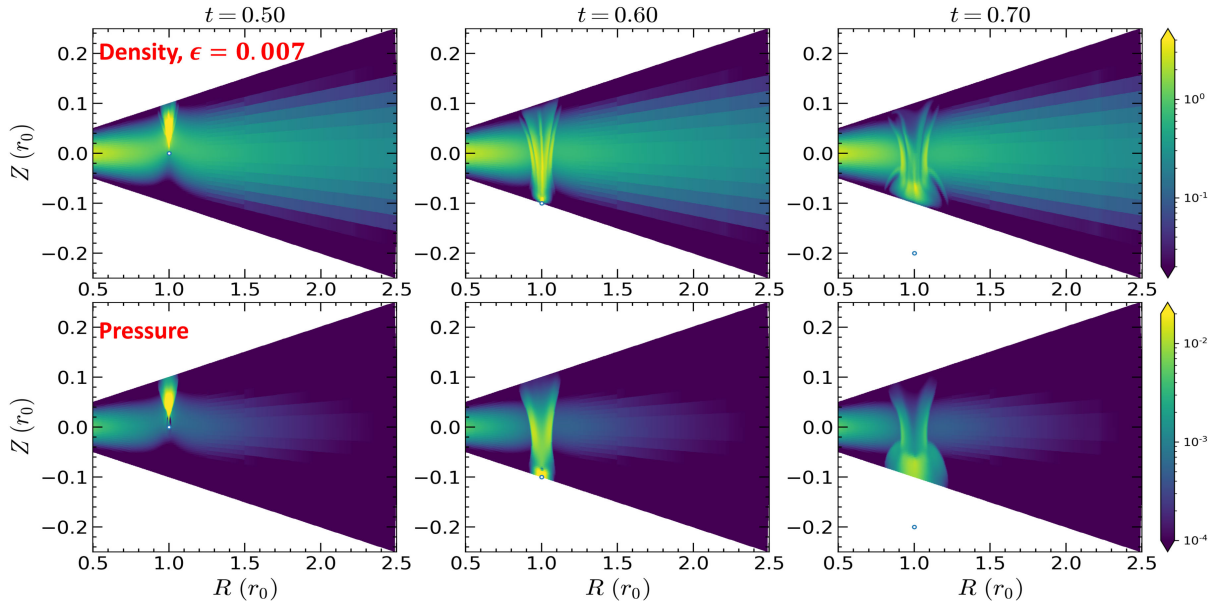

FIG. 12. Density (upper panels) and pressure (lower panels) distribution in the $R-Z$ plane with a slice along the azimuth of the colliding object, i.e., $\phi = 0$. The colliding object has a softening/sink radius of $\epsilon = 0.007 r_0$. Different columns correspond to different times in units of the local Keplerian orbital period. The small open circle denotes the position of the colliding object.

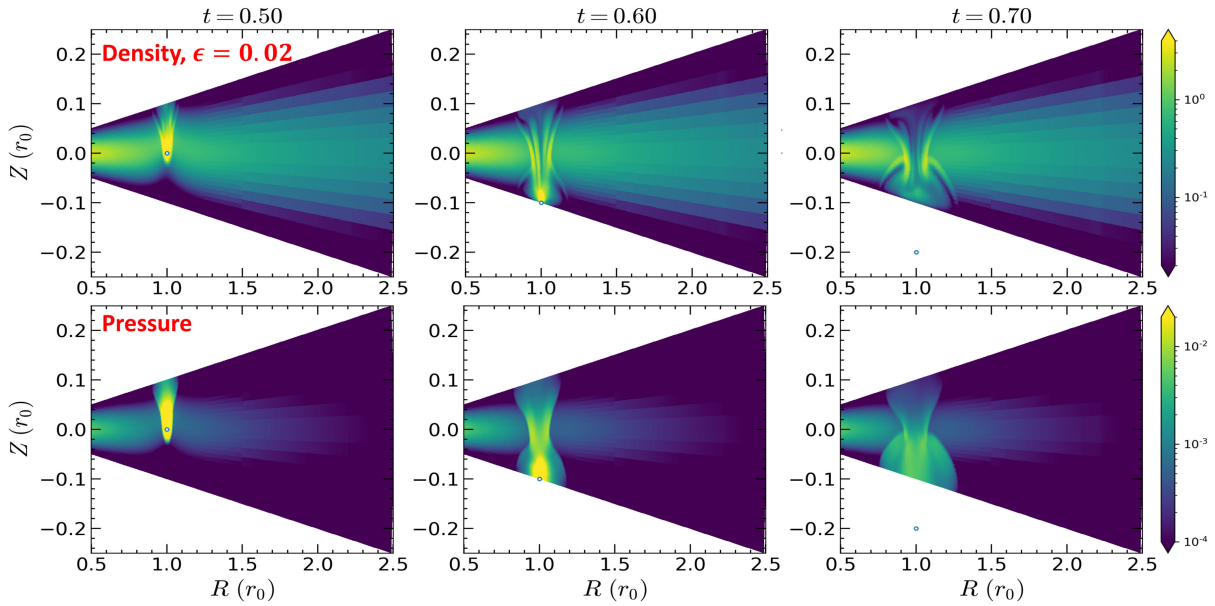

FIG. 13. Similar to Fig. 12, but with $\epsilon = 0.02 r_0$.

It is clearly seen that the perturbation is most prominent in the upper half of the disk before the collision and then becomes stronger later at the lower half of the disk. As expected, there is a time delay between the peaks of the perturbed disk mass for the upper and lower disks, though this time the delay may suffer from the boundary condition effect in the θ direction as we do not simulate the full θ domain of the disk. The difference of the integrated mass is not that large, although the local asymmetry of the density and pressure shown in Figs. 12 and 13 is stronger.

In addition, along the moving direction of the SMO, the burst actually consists of two components: a "precursor" burst at the moment of the shock breaking out of the disk surface ($t = 0.6$ in Figs. 12 and 13) followed by a main burst sourced by the heated gas in the shocked column. In either light curve model, the former component is not modeled, and this is a possible reason that $F_t > 1$.

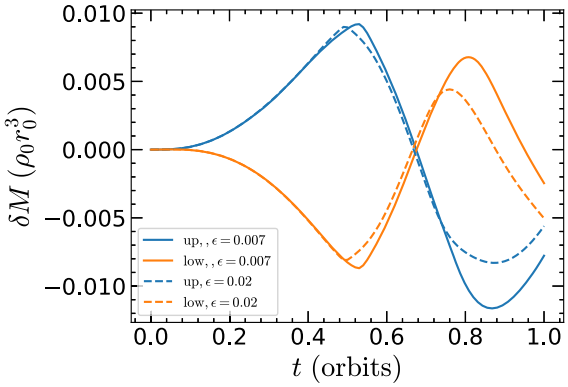

FIG. 14. Perturbed disk mass (subtracted from the initial disk mass) as a function of time. Solid lines correspond to the case with a softening/sink radius of $\epsilon = 0.007 r_0$, while the dashed lines are the case of $\epsilon = 0.02 r_0$. Blue (orange) lines are integrated over the upper (lower) half of the disk.

[1] Luming Sun, Xinwen Shu, and Tinggui Wang, RX J1301.9 + 2747: A highly variable Seyfert galaxy with extremely soft x-ray emission, Astrophys. J. **768**, 167 (2013).

[2] Margherita Giustini, Giovanni Miniutti, and Richard D. Saxton, X-ray quasi-periodic eruptions from the galactic nucleus of RX J1301.9 + 2747, Astron. Astrophys. **636**, L2 (2020).

[3] R. Arcodia *et al.*, X-ray quasi-periodic eruptions from two previously quiescent galaxies, Nature (London) **592**, 704 (2021).

[4] R. Arcodia, G. Miniutti, G. Ponti, J. Buchner, M. Giustini, A. Merloni, K. Nandra, F. Vincentelli, E. Kara, M. Salvato, and D. Pasham, The complex time and energy evolution of quasi-periodic eruptions in eRO-QPE1, Astron. Astrophys. **662**, A49 (2022).

[5] Joheen Chakraborty, Erin Kara, Megan Masterson, Margherita Giustini, Giovanni Miniutti, and Richard Saxton, Possible x-ray quasi-periodic eruptions in a tidal disruption event candidate, Astrophys. J. Lett. **921**, L40 (2021).

[6] T. Wevers, D. R. Pasham, P. Jalan, S. Rakshit, and R. Arcodia, Host galaxy properties of quasi-periodically erupting x-ray sources, Astron. Astrophys. **659**, L2 (2022).

[7] G. Miniutti, M. Giustini, R. Arcodia, R. D. Saxton, J. Chakraborty, A. M. Read, and E. Kara, Alive and kicking: A new QPE phase in GSN 069 revealing a quiescent luminosity threshold for QPEs, Astron. Astrophys. **674**, L1 (2023).

[8] X. W. Shu, S. S. Wang, L. M. Dou, N. Jiang, J. X. Wang, and T. G. Wang, A long decay of x-ray flux and spectral evolution in the supersoft active galactic nucleus GSN 069, Astrophys. J. Lett. **857**, L16 (2018).

[9] Zhenfeng Sheng, Tinggui Wang, Gary Ferland, Xinwen Shu, Chenwei Yang, Ning Jiang, and Yang Chen, Evidence of a tidal-disruption event in GSN 069 from the abnormal carbon and nitrogen abundance ratio, Astrophys. J. Lett. **920**, L25 (2021).

[10] E. Quintin, N. A. Webb, S. Guillot, G. Miniutti, E. S. Kammoun, M. Giustini, R. Arcodia, G. Soucail, N. Clerc, R. Amato, and C. B. Markwardt, Tormund's return: Hints of quasi-periodic eruption features from a recent optical tidal disruption event, Astron. Astrophys. **675**, A152 (2023).

[11] G. Miniutti, M. Giustini, R. Arcodia, R. D. Saxton, A. M. Read, S. Bianchi, and K. D. Alexander, Repeating tidal disruptions in GSN 069: Long-term evolution and constraints on quasi-periodic eruptions' models, Astron. Astrophys. **670**, A93 (2023).

[12] Tingting Liu, Massive black holes flaring up time and again, Nat. Astron. **5**, 438 (2021).

[13] A. Raj and C. J. Nixon, Disk tearing: Implications for black hole accretion and AGN variability, Astrophys. J. **909**, 82 (2021).

[14] Xin Pan, Shuang-Liang Li, Xinwu Cao, Giovanni Miniutti, and Minfeng Gu, A disk instability model for the quasi-periodic eruptions of GSN 069, Astrophys. J. Lett. **928**, L18 (2022).

[15] Xin Pan, Shuang-Liang Li, and Xinwu Cao, Application of the disk instability model to all quasiperiodic eruptions, Astrophys. J. **952**, 32 (2023).

[16] Karamveer Kaur, Nicholas C. Stone, and Shmuel Gilbaum, Magnetically dominated discs in tidal disruption events and quasi-periodic eruptions, Mon. Not. R. Astron. Soc. **524**, 1269 (2023).

[17] Marzena Śniegowska, Mikołaj Grzędzielski, Bożena Czerny, and Agnieszka Janiuk, Modified models of radiation pressure instability applied to 10, 10^5, and $10 M_\odot$ accreting black holes, Astron. Astrophys. **672**, A19 (2023).

[18] Adam Ingram, Sara E. Motta, Suzanne Aigrain, and Aris Karastergiou, A self-lensing binary massive black hole interpretation of quasi-periodic eruptions, Mon. Not. R. Astron. Soc. **503**, 1703 (2021).

[19] Andrew King, GSN 069—A tidal disruption near miss, Mon. Not. R. Astron. Soc. **493**, L120 (2020).
[20] Andrew King, Quasi-periodic eruptions from galaxy nuclei, Mon. Not. R. Astron. Soc. **515**, 4344 (2022).
[21] Andrew King, Angular momentum transfer in QPEs from galaxy nuclei, Mon. Not. R. Astron. Soc. **520**, L63 (2023).
[22] Xian Chen, Yu Qiu, Shuo Li, and F. K. Liu, Milli-hertz gravitational-wave background produced by quasiperiodic eruptions, Astrophys. J. **930**, 122 (2022).
[23] Mengye Wang, Jinjing Yin, Yiqiu Ma, and Qingwen Wu, A model for the possible connection between a tidal disruption event and quasi-periodic eruption in GSN 069, Astrophys. J. **933**, 225 (2022).
[24] Z. Y. Zhao, Y. Y. Wang, Y. C. Zou, F. Y. Wang, and Z. G. Dai, Quasi-periodic eruptions from the helium envelope of hydrogen-deficient stars stripped by supermassive black holes, Astron. Astrophys. **661**, A55 (2022).
[25] Brian D. Metzger, Nicholas C. Stone, and Shmuel Gilbaum, Interacting stellar EMRIs as sources of quasi-periodic eruptions in galactic nuclei, Astrophys. J. **926**, 101 (2022).
[26] Wenbin Lu and Eliot Quataert, Quasi-periodic eruptions from mildly eccentric unstable mass transfer in galactic nuclei, Mon. Not. R. Astron. Soc. **524**, 6247 (2023).
[27] Julian H. Krolik and Itai Linial, Quasiperiodic erupters: A stellar mass-transfer model for the radiation, Astrophys. J. **941**, 24 (2022).
[28] Itai Linial and Re'em Sari, Unstable mass transfer from a main-sequence star to a supermassive black hole and quasiperiodic eruptions, Astrophys. J. **945**, 86 (2023).
[29] Petra Suková, Michal Zajaček, Vojtěch Witzany, and Vladimír Karas, Stellar transits across a magnetized accretion torus as a mechanism for plasmoid ejection, Astrophys. J. **917**, 43 (2021).
[30] Jingtao Xian, Fupeng Zhang, Liming Dou, Jiasheng He, and Xinwen Shu, X-ray quasi-periodic eruptions driven by star-disk collisions: Application to GSN 069 and probing the spin of massive black holes, Astrophys. J. Lett. **921**, L32 (2021).
[31] Hiromichi Tagawa and Zoltán Haiman, Flares from stars crossing active galactic nuclei disks on low-inclination orbits, Mon. Not. R. Astron. Soc. **526**, 69 (2023).
[32] Itai Linial and Brian D. Metzger, EMRI + TDE = QPE: Periodic x-ray flares from star-disk collisions in galactic nuclei, Astrophys. J. **957**, 34 (2023).
[33] Alessia Franchini, Matteo Bonetti, Alessandro Lupi, Giovanni Miniutti, Elisa Bortolas, Margherita Giustini, Massimo Dotti, Alberto Sesana, Riccardo Arcodia, and Taeho Ryu, Quasi-periodic eruptions from impacts between the secondary and a rigidly precessing accretion disc in an extreme mass-ratio inspiral system, Astron. Astrophys. **675**, A100 (2023).
[34] G. Miniutti, R. D. Saxton, M. Giustini, K. D. Alexander, R. P. Fender, I. Heywood, I. Monageng, M. Coriat, A. K. Tzioumis, A. M. Read, C. Knigge, P. Gandhi, M. L. Pretorius, and B. Agís-González, Nine-hour x-ray quasi-periodic eruptions from a low-mass black hole galactic nucleus, Nature (London) **573**, 381 (2019).
[35] Itai Linial and Brian D. Metzger, Ultraviolet quasi-periodic eruptions from star-disk collisions in galactic nuclei, Astrophys. J. Lett. **963**, L1 (2024).
[36] W. D. Arnett, Analytic solutions for light curves of supernovae of Type II, Astrophys. J. **237**, 541 (1980).
[37] Harry J. Lehto and Mauri J. Valtonen, OJ 287 outburst structure and a binary black hole model, Astrophys. J. **460**, 207 (1996).
[38] P. Pihajoki, Black hole accretion disc impacts, Mon. Not. R. Astron. Soc. **457**, 1145 (2016).
[39] Ning Jiang, Huan Yang, Tinggui Wang, Jiazheng Zhu, Zhenwei Lyu, Liming Dou, Yibo Wang, Jianguo Wang, Zhen Pan, Hui Liu, Xinwen Shu, and Zhenya Zheng, Ticktock: The imminent merger of a supermassive black hole binary, arXiv:2201.11633.
[40] Pavel B. Ivanov, Igor V. Igumenshchev, and Igor D. Novikov, Hydrodynamics of black hole-accretion disk collision, Astrophys. J. **507**, 131 (1998).
[41] N. I. Shakura and R. A. Sunyaev, Black holes in binary systems. Observational appearance, Astron. Astrophys. **24**, 337 (1973).
[42] Bence Kocsis, Nicolás Yunes, and Abraham Loeb, Observable signatures of extreme mass-ratio inspiral black hole binaries embedded in thin accretion disks, Phys. Rev. D **84**, 024032 (2011).
[43] S. Chandrasekhar, Dynamical friction. I. General considerations: The coefficient of dynamical friction, Astrophys. J. **97**, 255 (1943).
[44] Y. Rephaeli and E. E. Salpeter, Flow past a massive object and the gravitational drag, Astrophys. J. **240**, 20 (1980).
[45] James Binney and Scott Tremaine, *Galactic Dynamics* (Princeton University Press, 1987).
[46] Eve C. Ostriker, Dynamical friction in a gaseous medium, Astrophys. J. **513**, 252 (1999).
[47] A. Shankar, W. Kley, and A. Burkert, Axisymmetric accretion flow past large, gravitating bodies, Astron. Astrophys. **274**, 955 (1993).
[48] Maximilian Ruffert and David Arnett, Three-dimensional hydrodynamic Bondi-Hoyle accretion. II. Homogeneous medium at Mach 3 with gamma = 5/3, Astrophys. J. **427**, 351 (1994).
[49] Richard Edgar, A review of Bondi-Hoyle-Lyttleton accretion, New Astron. Rev. **48**, 843 (2004).
[50] Damien Chapon, Lucio Mayer, and Romain Teyssier, Hydrodynamics of galaxy mergers with supermassive black holes: Is there a last parsec problem?, Mon. Not. R. Astron. Soc. **429**, 3114 (2013).
[51] Daniel Thun, Rolf Kuiper, Franziska Schmidt, and Wilhelm Kley, Dynamical friction for supersonic motion in a homogeneous gaseous medium, Astron. Astrophys. **589**, A10 (2016).
[52] R. Hunt, A fluid dynamical study of the accretion process, Mon. Not. R. Astron. Soc. **154**, 141 (1971).
[53] R. Hunt, Accretion of gas having specific heat ratio 3/3 by a moving gravitating body, Mon. Not. R. Astron. Soc. **188**, 83 (1979).
[54] E. Shima, T. Matsuda, H. Takeda, and K. Sawada, Hydrodynamic calculations of axisymmetric accretion flow, Mon. Not. R. Astron. Soc. **217**, 367 (1985).

[55] M. Ruffert, Three-dimensional hydrodynamic Bondi-Hoyle accretion. V. Specific heat ratio 1.01, nearly isothermal flow, Astron. Astrophys. **311**, 817 (1996).
[56] J. P. Norris, J. T. Bonnell, D. Kazanas, J. D. Scargle, J. Hakkila, and T. W. Giblin, Long-lag, wide-pulse gamma-ray bursts, Astrophys. J. **627**, 324 (2005).
[57] S. Chandrasekhar, *The Mathematical Theory of Black Holes* (Clarendon Press, 1983).
[58] Irwin I. Shapiro, Fourth test of general relativity, Phys. Rev. Lett. **13**, 789 (1964).
[59] Joshua S. Speagle, DYNESTY: A dynamic nested sampling package for estimating Bayesian posteriors and evidences, Mon. Not. R. Astron. Soc. **493**, 3132 (2020).
[60] Michael J. Williams, *nessai: Nested sampling with artificial intelligence* (2021).
[61] Gregory Ashton *et al.*, BILBY: A user-friendly Bayesian inference library for gravitational-wave astronomy, Astrophys. J. Suppl. Ser. **241**, 27 (2019).
[62] L. Strüder *et al.*, The European photon imaging camera on XMM-Newton: The pn-CCD camera, Astron. Astrophys. **365**, L18 (2001).
[63] K. A. Arnaud, *XSPEC: The First Ten Years, in Astronomical Data Analysis Software and Systems V*, Astronomical Society of the Pacific Conference Series Vol. 101, edited by George H. Jacoby and Jeannette Barnes (1996), p. 17.
[64] Kishore C. Patra, Wenbin Lu, Yilun Ma, Eliot Quataert, Giovanni Miniutti, Marco Chiaberge, and Alexei V. Filippenko, Constraints on the narrow-line region of the x-ray quasi-periodic eruption source GSN069, arXiv:2310.05574.
[65] Zhen Pan, Zhenwei Lyu, and Huan Yang, Mass-gap extreme mass ratio inspirals, Phys. Rev. D **105**, 083005 (2022).
[66] Zhen Pan and Huan Yang, Supercritical accretion of stellar-mass compact objects in active galactic nuclei, Astrophys. J. **923**, 173 (2021).
[67] Zhen Pan and Huan Yang, Formation rate of extreme mass ratio inspirals in active galactic nuclei, Phys. Rev. D **103**, 103018 (2021).
[68] Zhen Pan, Zhenwei Lyu, and Huan Yang, Wet extreme mass ratio inspirals may be more common for spaceborne gravitational wave detection, Phys. Rev. D **104**, 063007 (2021).
[69] Jianxiang Wang and David Merritt, Revised rates of stellar disruption in galactic nuclei, Astrophys. J. **600**, 149 (2004).
[70] Nicholas C. Stone and Brian D. Metzger, Rates of stellar tidal disruption as probes of the supermassive black hole mass function, Mon. Not. R. Astron. Soc. **455**, 859 (2016).
[71] M. Liska, C. Hesp, A. Tchekhovskoy, A. Ingram, M. van der Klis, and S. Markoff, Formation of precessing jets by tilted black hole discs in 3D general relativistic MHD simulations, Mon. Not. R. Astron. Soc. **474**, L81 (2018).
[72] K. Chatterjee, Z. Younsi, M. Liska, A. Tchekhovskoy, S. B. Markoff, D. Yoon, D. van Eijnatten, C. Hesp, A. Ingram, and M. B. M. van der Klis, Observational signatures of disc and jet misalignment in images of accreting black holes, Mon. Not. R. Astron. Soc. **499**, 362 (2020).
[73] Koushik Chatterjee, Matthew Liska, Alexander Tchekhovskoy, and Sera Markoff, Misaligned magnetized accretion flows onto spinning black holes: Magneto-spin alignment, outflow power and intermittent jets, arXiv:2311.00432.
[74] Nicholas Stone and Abraham Loeb, Observing Lense-Thirring precession in tidal disruption flares, Phys. Rev. Lett. **108**, 061302 (2012).
[75] Alessia Franchini, Giuseppe Lodato, and Stefano Facchini, Lense-Thirring precession around supermassive black holes during tidal disruption events, Mon. Not. R. Astron. Soc. **455**, 1946 (2016).
[76] Itai Linial and Eliot Quataert, Period evolution of repeating transients in galactic nuclei, Mon. Not. R. Astron. Soc. **527**, 4317 (2024).
[77] Jean J. Somalwar *et al.*, The first systematically identified repeating partial tidal disruption event, arXiv:2310.03782.
[78] Nicholas C. Stone, Eugene Vasiliev, Michael Kesden, Elena M. Rossi, Hagai B. Perets, and Pau Amaro-Seoane, Rates of stellar tidal disruption, Space Sci. Rev. **216**, 35 (2020).
[79] M. Cufari, Eric R. Coughlin, and C. J. Nixon, Using the Hills mechanism to generate repeating partial tidal disruption events and ASASSN-14ko, Astrophys. J. Lett. **929**, L20 (2022).
[80] M. Coleman Miller, Marc Freitag, Douglas P. Hamilton, and Vanessa M. Lauburg, Binary encounters with supermassive black holes: Zero-eccentricity LISA events, Astrophys. J. Lett. **631**, L117 (2005).
[81] Clovis Hopman and Tal Alexander, The orbital statistics of stellar inspiral and relaxation near a massive black hole: Characterizing gravitational wave sources, Astrophys. J. **629**, 362 (2005).
[82] Miguel Preto and Pau Amaro-Seoane, On strong mass segregation around a massive black hole: Implications for lower-frequency gravitational-wave astrophysics, Astrophys. J. Lett. **708**, L42 (2010).
[83] Ben Bar-Or and Tal Alexander, Steady-state relativistic stellar dynamics around a massive black hole, Astrophys. J. **820**, 129 (2016).
[84] Stanislav Babak, Jonathan Gair, Alberto Sesana, Enrico Barausse, Carlos F. Sopuerta, Christopher P. L. Berry, Emanuele Berti, Pau Amaro-Seoane, Antoine Petiteau, and Antoine Klein, Science with the space-based interferometer LISA. V. Extreme mass-ratio inspirals, Phys. Rev. D **95**, 103012 (2017).
[85] Pau Amaro-Seoane, Relativistic dynamics and extreme mass ratio inspirals, Living Rev. Relativity **21**, 4 (2018).
[86] Luca Broggi, Elisa Bortolas, Matteo Bonetti, Alberto Sesana, and Massimo Dotti, Extreme mass ratio inspirals and tidal disruption events in nuclear clusters—I. Time-dependent rates, Mon. Not. R. Astron. Soc. **514**, 3270 (2022).
[87] Yael Raveh and Hagai B. Perets, Extreme mass-ratio gravitational-wave sources: Mass segregation and post binary tidal-disruption captures, Mon. Not. R. Astron. Soc. **501**, 5012 (2021).
[88] Günter Sigl, Jeremy Schnittman, and Alessandra Buonanno, Gravitational-wave background from compact

objects embedded in active galactic nuclei accretion disks, Phys. Rev. D **75**, 024034 (2007).
[89] Yuri Levin, Starbursts near supermassive black holes: Young stars in the Galactic Centre, and gravitational waves in LISA band, Mon. Not. R. Astron. Soc. **374**, 515 (2007).
[90] Andrea Derdzinski and Lucio Mayer, In situ extreme mass ratio inspirals via subparsec formation and migration of stars in thin, gravitationally unstable AGN discs, Mon. Not. R. Astron. Soc. **521**, 4522 (2023).
[91] Yihan Wang, Zhaohuan Zhu, and Douglas N. C. Lin, Stellar/BH population in AGN disks: Direct binary formation from capture objects in nuclei clusters, Mon. Not. R. Astron. Soc. **528**, 4958 (2024).
[92] Yihan Wang, Douglas N. C. Lin, Bing Zhang, and Zhaohuan Zhu, Changing-Look AGN behaviour induced by disk-captured tidal disruption events, Astrophys. J. Lett. **962**, L7 (2024).
[93] Lyman Spitzer, *Dynamical Evolution of Globular Clusters* (Princeton University Press, 1987).
[94] Scott Tremaine, Karl Gebhardt, Ralf Bender, Gary Bower, Alan Dressler, S. M. Faber, Alexei V. Filippenko, Richard Green, Carl Grillmair, Luis C. Ho, John Kormendy, Tod R. Lauer, John Magorrian, Jason Pinkney, and Douglas Richstone, The slope of the black hole mass versus velocity dispersion correlation, Astrophys. J. **574**, 740 (2002).
[95] Kayhan Gültekin, Douglas O. Richstone, Karl Gebhardt, Tod R. Lauer, Scott Tremaine, M. C. Aller, Ralf Bender, Alan Dressler, S. M. Faber, Alexei V. Filippenko, Richard Green, Luis C. Ho, John Kormendy, John Magorrian, Jason Pinkney, and Christos Siopis, The M-σ and M-L relations in galactic bulges, and determinations of their intrinsic scatter, Astrophys. J. **698**, 198 (2009).
[96] P. C. Peters, Gravitational radiation and the motion of two point masses, Phys. Rev. **136**, B1224 (1964).
[97] J. N. Bahcall and R. A. Wolf, Star distribution around a massive black hole in a globular cluster., Astrophys. J. **209**, 214 (1976).
[98] Hidekazu Tanaka, Taku Takeuchi, and William R. Ward, Three-dimensional interaction between a planet and an isothermal gaseous disk. I. Corotation and Lindblad torques and planet migration, Astrophys. J. **565**, 1257 (2002).
[99] Hidekazu Tanaka and William R. Ward, Three-dimensional interaction between a planet and an isothermal gaseous disk. II. Eccentricity waves and bending waves, Astrophys. J. **602**, 388 (2004).
[100] F. Verbunt and E. S. Phinney, Tidal circularization and the eccentricity of binaries containing giant stars, Astron. Astrophys. **296**, 709 (1995).
[101] Omer Blaes, Man Hoi Lee, and Aristotle Socrates, The Kozai mechanism and the evolution of binary supermassive black holes, Astrophys. J. **578**, 775 (2002).
[102] Bin Liu, Diego J. Muñoz, and Dong Lai, Suppression of extreme orbital evolution in triple systems with short-range forces, Mon. Not. R. Astron. Soc. **447**, 747 (2015).
[103] Jane Lixin Dai, Giuseppe Lodato, and Roseanne Cheng, The physics of accretion discs, winds and jets in tidal disruption events, Space Sci. Rev. **217**, 12 (2021).
[104] Maximiliano Isi, Katerina Chatziioannou, and Will M. Farr, Hierarchical test of general relativity with gravitational waves, Phys. Rev. Lett. **123**, 121101 (2019).
[105] P. A. Evans, C. J. Nixon, S. Campana, P. Charalampopoulos, D. A. Perley, A. A. Breeveld, K. L. Page, S. R. Oates, R. A. J. Eyles-Ferris, D. B. Malesani, L. Izzo, M. R. Goad, P. T. O'Brien, J. P. Osborne, and B. Sbarufatti, Monthly quasi-periodic eruptions from repeated stellar disruption by a massive black hole, Nat. Astron. **7**, 1368 (2023).
[106] Muryel Guolo, Dheeraj R. Pasham, Michal Zajaček, Eric R. Coughlin, Suvi Gezari, Petra Suková, Thomas Wevers, Vojtěch Witzany, Francesco Tombesi, Sjoert van Velzen, Kate D. Alexander, Yuhan Yao, Riccardo Arcodia, Vladimír Karas, James C. A. Miller-Jones, Ronald Remillard, Keith Gendreau, and Elizabeth C. Ferrara, X-ray eruptions every 22 days from the nucleus of a nearby galaxy, Nat. Astron. **8**, 347 (2024).
[107] Eiichiro Kokubo, Keiko Yoshinaga, and Junichiro Makino, On a time-symmetric Hermite integrator for planetary N-body simulation, Mon. Not. R. Astron. Soc. **297**, 1067 (1998).
[108] James M. Stone, Kengo Tomida, Christopher J. White, and Kyle G. Felker, The Athena++ Adaptive mesh refinement framework: Design and magnetohydrodynamic solvers, Astrophys. J. Suppl. Ser. **249**, 4 (2020).